



Dating prograde metamorphism: U–Pb geochronology of allanite and REE-rich epidote in the Eastern Alps

S. Stumpf^{1,2} · E. Skrzypek¹ · K. Stüwe¹

Received: 18 October 2023 / Accepted: 6 April 2024 / Published online: 29 May 2024
© The Author(s) 2024

Abstract

We use U–Pb dating of allanite and REE-rich epidote in three polymetamorphosed units from the Eastern Alps to constrain the timing of prograde metamorphism. All three units (Ennstal, Wölz and Rappold Complex) record several metamorphic cycles (Variscan, Permian and Eoalpine) and presently define an Eoalpine (Cretaceous) metamorphic field gradient from lower greenschist to amphibolite facies. For U–Pb data, a method is introduced to test the magnitude of ²³⁰Th disequilibrium and potentially approximate the Th/U ratio of the reservoir out of which allanite and REE-rich epidote grew. We also show that the modelled stability of epidote-group minerals in the REE-free MnNCKFMASH and MnNCKFMASHTO systems and REE-bearing systems is nearly identical. By combining the stability fields of (clino-)zoisite and epidote modelled in REE-free systems with known geothermal gradients for the region, REE-rich epidote growth is constrained to 200–450 °C and 0.2–0.8 GPa during prograde metamorphism. In the Rappold Complex, allanite cores yield a Variscan age of ca. 327 Ma. In the Ennstal and Wölz Complex, allanite growth during the Permian event occurred at ca. 279–286 Ma. Importantly, recrystallized allanite laths and REE-rich epidote overgrowths in samples from all three units yield prograde Eoalpine ages of ca. 100 Ma, even though these units subsequently reached different peak conditions, most likely at different times. This suggests that all units were buried roughly at the same time during the onset of Eoalpine continental subduction. This interpretation leaves room for the model proposing that diachronous peak metamorphic conditions reported for the field gradient may be related to the inertia of thermal equilibration rather than tectonic processes.

Keywords Allanite · Epidote · U–Pb dating · Prograde metamorphism · Field gradient

Introduction

Robust geochronological constraints for different stages of a metamorphic pressure–temperature (*P–T*) path are crucial for reconstructing the tectonic evolution of collisional orogens (e.g., Foster et al. 2004). However, the most commonly used geochronometers hardly give information on the early stage of a *P–T* evolution. U–Pb systematics of zircon, by far the most popular, will mainly record the timing of peak *P–T* conditions (see Rubatto 2017 for a review), if not

the onset of cooling from high-*T* conditions (e.g., Roberts and Finger 1997; Yakymchuk 2023). Monazite, a versatile accessory mineral (Hetherington and Dumond 2013), can yield information on the prograde path but its high reactivity will tend to erase this record (e.g., Seydoux-Guillaume et al. 2003; Skrzypek et al. 2018). Micas, although they form at relatively low *P–T* conditions, suffer from Ar loss and are prone to age resetting above ~350 °C; they may record peak high-pressure conditions (e.g., Villa et al. 2022), but commonly document late stages of a *P–T* history (see Schaen et al 2020).

Allanite is a Rare Earth Element (REE)-bearing epidote (Gieré and Sorensen 2004) and a potential tool to date the prograde segment of *P–T* loops (e.g., Janots et al. 2009; Airaghi et al. 2019). It is known to crystallize at an early stage of metamorphism and incorporates U and Th, which allows for Th–U–Pb dating by various methods (Gregory et al. 2007). The U–Pb isotopic system in allanite is thought to remain closed under greenschist and amphibolite facies

Communicated by Dante Canil.

✉ S. Stumpf
sebastian.stumpf@unibe.ch

¹ Institute of Earth Sciences, University of Graz,
Universitätsplatz 2, A-8010 Graz, Austria

² Institute of Geological Sciences, University of Bern,
Baltzerstraße 1+3, CH-3012 Bern, Switzerland

conditions (< 650 °C), and therefore can yield the age of initial allanite crystallization (Heaman and Parrish 1991; Parrish 2001). The exact P – T conditions at which metamorphic allanite or REE-rich epidote initially grows are still unclear. Some studies document crystallization of metamorphic allanite after detrital or low-grade monazite at lower greenschist facies conditions, while allanite is replaced again by monazite in the upper amphibolite facies (Smith and Barreiro 1990; Wing et al. 2003; Janots et al. 2008; Gasser et al. 2012a). As such, allanite ages may document a point on the prograde path in the greenschist facies (Goswami-Banerjee and Robyr 2015).

The lack of geochronological information on prograde metamorphism is particularly conspicuous in the Austroalpine nappe stack of the Eastern European Alps. Numerous constraints are ascribed to the thermal peak (Sm–Nd, Rb–Sr, Lu–Hf, U–Pb; Thöni et al. 2008) or the subsequent cooling path (Ar–Ar on micas; Neubauer et al. 1995; Wiesinger et al. 2006), but little is known about the prograde P – T segment. At present, the overall duration of the metamorphic evolution can only be derived from protolith ages (e.g., U–Pb detrital zircon ages; Gasser et al. 2012b). We therefore use a transect across the former continental subduction zone to illustrate the importance of allanite/REE-rich epidote for dating prograde metamorphism. We study the Austroalpine nappe stack located in Eastern Austria, where polymetamorphosed rocks are exposed along a metamorphic field gradient from lower greenschist to amphibolite facies over some 40 km (Fig. 1). Chemical compositions and textures of allanite partly surrounded by REE-rich epidote rims in metapelitic rock samples are documented in three different units. These petrological observations are used to guide in situ dating by laser ablation-inductively coupled plasma-mass spectrometry (LA-ICP-MS) in allanite cores and REE-rich epidote rim domains. Furthermore, we compare thermodynamic modelling results in REE-bearing and REE-free systems and estimate P – T conditions of REE-rich epidote growth by combining pseudosection modelling with published metamorphic gradients. We also present a new method to evaluate the effect of ^{230}Th disequilibrium on age results, and potentially assess the Th/U ratio of the reservoir out of which allanite and REE-rich epidote grew. We use the new U–Pb dates to constrain aspects of the early subduction process.

Geology of the Eastern Alps

The Eastern Alps extend over ~500 km from the easternmost part of Switzerland to Eastern Austria and Northern Slovenia. They consist predominantly of the Austroalpine nappes derived from the Mesozoic Adriatic plate. The Austroalpine nappe stack is divided into the Upper and Lower

Austroalpine nappes. This study focuses on units from the Upper Austroalpine nappes: the Koralpe–Wölz and the Tirolic–Noric nappe systems (Fig. 1) (Schmid et al. 2004). Although these nappe systems acquired their final structure, metamorphic overprint and tectonic position during Alpine orogeny and Cretaceous nappe stacking, they show evidence of earlier Variscan and Permian metamorphic events (Froitzheim et al. 2008). While the Variscan event was associated with large-scale magmatism and metamorphism and is rather unrelated to Alpine orogeny, the tectonics of the Permian event had major consequences for the onset of the Eoalpine orogenic cycle (Schuster and Stüwe 2008; Kroner and Romer 2013). The onset of subduction during Alpine orogeny occurred within the Adriatic plate and caused further separation of the Upper Austroalpine into units that belonged to the upper and lower plate, respectively (Fig. 2) (Schmid et al. 2004; Stüwe and Schuster 2010). The Koralpe–Wölz and Tirolic–Noric nappe systems formed in the lower plate during this intracontinental subduction. While the Tirolic–Noric nappe system remained at shallow depth and underwent low-grade metamorphism, the Koralpe–Wölz nappe system experienced up to eclogite facies metamorphism in its southern part and represents an extruded high pressure wedge (Tenczer and Stüwe 2003; Schmid et al. 2004; Thöni et al. 2008; Hauke et al. 2019).

We investigate three units at the northern margin of the Austroalpine nappe stack that were all part of the lower plate. From north to south the Ennstal Complex, Wölz Complex and Rappold Complex show increasing metamorphic grade from lower greenschist to amphibolite facies conditions (Fig. 1) (Faryad and Hoinkes 2003; Froitzheim et al. 2008). The Ennstal Complex is mostly composed of phyllite with greenschist intercalations and its association with the Tirolic–Noric nappe system or Koralpe–Wölz nappe system is debated. Froitzheim et al. (2008) use the continuous metamorphic gradient to propose that the Ennstal Complex belongs to the Koralpe–Wölz nappe system but new data suggest that it is part of the Tirolic–Noric nappe system (Stumpf 2023). Both the Wölz and Rappold Complexes belong to the Koralpe–Wölz nappe system; they consist of micaschist with single- and two-phase garnet, marble and amphibolite. An Ordovician deposition age is proposed for the Wölz Complex based on Sr isotopes in marbles (Pühr 2013). The successive metamorphic events recognized in the Ennstal, Wölz and Rappold Complexes are summarized below.

Variscan cycle (Carboniferous)

In the Koralpe–Wölz nappe system, Variscan metamorphic ages obtained by Th–U–Pb monazite and Lu–Hf garnet-whole rock dating of metapelite and eclogite lie in the range 335–310 Ma (Krenn et al. 2012; Schulz 2017; Hauke et al. 2019). Gaidies et al. (2006, 2008) proposed

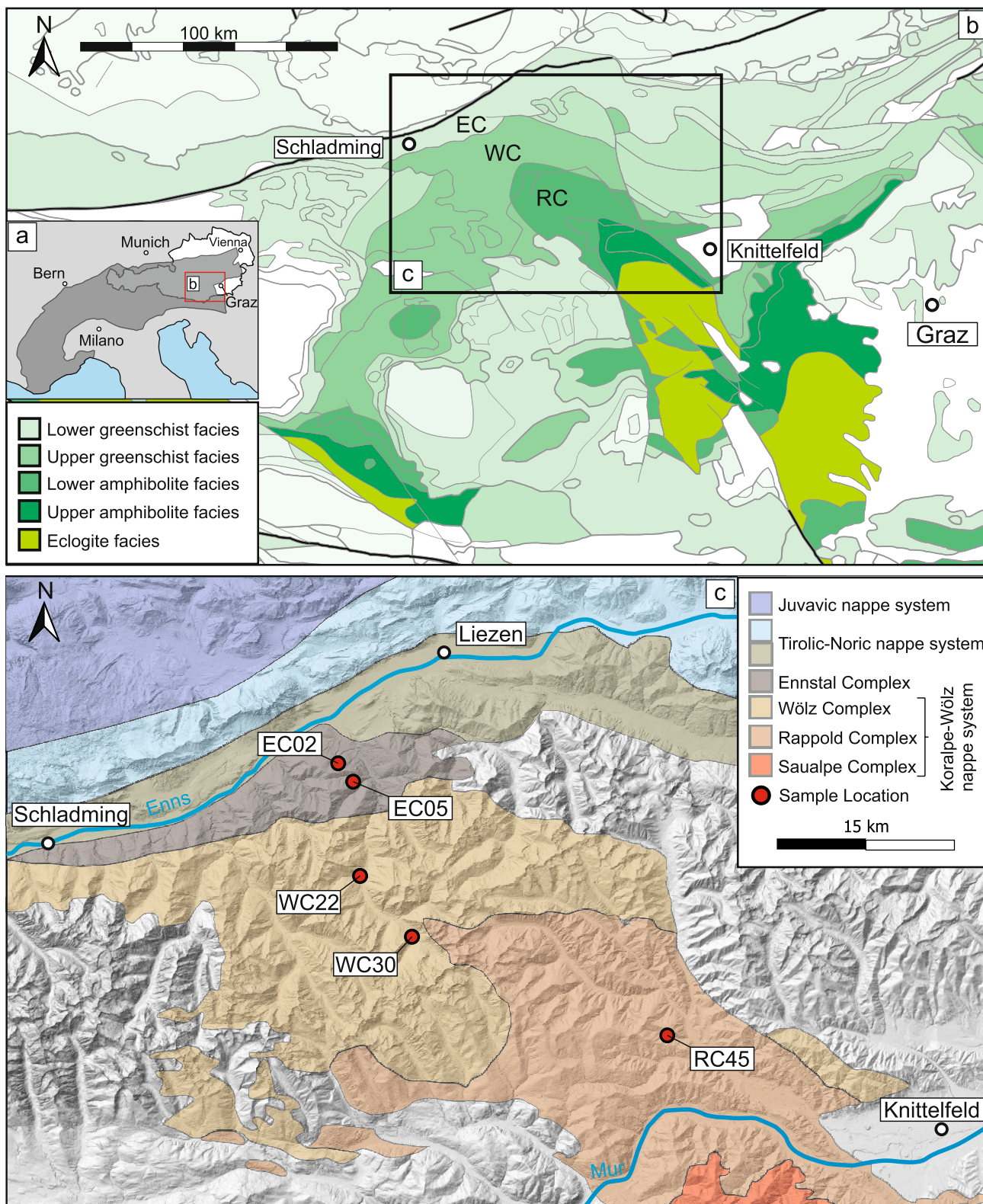


Fig. 1 a Overview map showing the location of the study area within the Alps (dark grey) and Austria (white). b Map depicting the distribution and grade of Eoalpine metamorphism in the Eastern Alps

(modified after Froitzheim et al. 2008). c Geology of the study area and sample locations

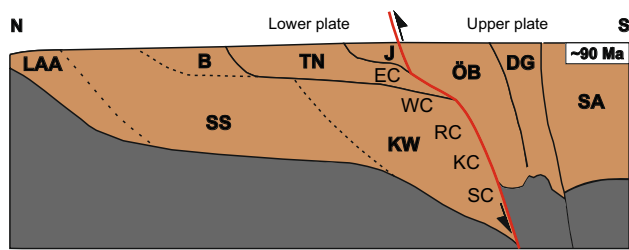


Fig. 2 Schematic geological profile showing the position of the Austroalpine nappe systems close to the peak of Eoalpine metamorphism. The respective positions of the EC, WC and RC are defining the Eoalpine metamorphic field gradient depicted in Fig. 1b. Modified after Stüwe and Schuster (2010). LAA=Lower Austroalpine, SS=Silvretta-Seckau nappe system, B=Bajuvaric nappe system, TN=Tirolitic-Noric nappe system, EC=Ennstal Complex, KW=Koralpe-Wölz nappe system, WC=Wölz Complex, RC=Rappold Complex, KC=Koralpe Complex, SC=Sausalpe Complex, ÖB=Ötztal-Bundschuh nappe system, DG=Drauzug-Gurktal nappe system, SA=South Alpine

a Variscan age for incipient garnet growth at ~ 525 °C and ~ 0.53 GPa using the innermost core of two-phase garnet from the Rappold Complex. Similar metamorphic conditions of ~ 540 °C and ~ 0.66 GPa were obtained for inclusions in a garnet core of possible Variscan age in a metapelite from the Rappold Complex (Faryad and Hoinkes 2003). No Variscan metamorphic or magmatic ages have been published for the Ennstal Complex.

Permian cycle

There is no age data for the Permian event in the Ennstal Complex. Recent Raman Spectroscopy of Carbonaceous Material (RSCM) data from Iglseider et al. (2022) indicates maximum metamorphic temperatures of 490–565 °C. These temperatures agree with the results of biotite-garnet thermometry (450 °C; Schlüter et al. 1984). It is suggested that these temperatures were reached during Permian metamorphism (Iglseider et al. 2022). The Permian event in the Koralpe-Wölz nappe system is characterized by low-*P*/high-*T* metamorphism and magmatic intrusions, and has been the focus of many geochronological and petrological studies (see summary by Schuster and Stüwe 2008). The majority of pegmatite intrusions and metamorphic rocks within the Koralpe-Wölz nappe system yield ages between 250 and 290 Ma (Krenn et al. 2012; Schulz 2017; Knoll et al. 2018 and references therein; Chang et al. 2023 and references therein). For this metamorphic event a high geothermal gradient of 45 °C/km is proposed (Schuster et al. 2001). Garnet isopleth thermobarometry shows that incipient garnet growth in metapelite from the Wölz Complex occurred at ~ 540 °C and 0.4–0.5 GPa (Gaidies et al. 2006; Bestel et al. 2009).

Eoalpine cycle (Cretaceous)

Peak *T* conditions for the Eoalpine overprint in the Ennstal Complex are thought to be lower than for the Permian event (< 490 –565 °C; Iglseider et al. 2022). Several geochronological and petrological studies were dedicated to Eoalpine metamorphism in the Koralpe-Wölz nappe system, especially in the high-grade parts (e.g., Koralpe Complex, Sausalpe Complex) where even several stages of the *P*–*T* loop are partially known (Thöni et al. 2008; Neubauer et al. 1995). Initial stages of garnet growth in the high-grade parts of the Koralpe-Wölz nappe system are estimated at ca. 95–94 Ma (Thöni et al. 2008). Incipient garnet growth occurred at 540–570 °C and 0.6–0.8 GPa in the Wölz and Rappold Complex (Gaidies et al. 2006; Bestel et al. 2009). Eclogite-facies peak metamorphic conditions of 630–740 °C and 2.2 GPa in the southern part of the Koralpe-Wölz nappe system (Sausalpe Complex) were reached at approximately 90–88 Ma (Thöni et al. 2008). Farther north, in the southern part of the Wölz Complex and the northern part of the Rappold Complex rocks underwent peak metamorphic conditions of 600–650 °C and 1.0–1.1 GPa along a geothermal gradient of 10–16 °C/km (Faryad and Hoinkes 2003). The prograde segment of this *P*–*T* evolution is largely unknown, in contrast to the cooling path. For example, $^{40}\text{Ar}/^{39}\text{Ar}$ ages recording cooling for the Koralpe-Wölz nappe system range from 85 to 78 Ma (Wiesinger et al. 2006; Neubauer et al. 1995) and fission track results date the end of Eoalpine metamorphism within the Koralpe-Wölz nappe system at ~ 50 Ma (Hejl 1997; Faupl and Wagerich 1996). The Eoalpine metamorphic cycle therefore lasted some 40 My from the onset of garnet growth to exhumation in the structurally lowest, high-grade metamorphic part of the Koralpe-Wölz nappe system.

Along the field gradient across the Koralpe-Wölz nappe system, a positive correlation between metamorphic grade and the age of peak metamorphism has been observed (Tenczer and Stüwe 2003). In other words, the metamorphic peak was reached earlier in low-grade and later in high-grade rocks. Stüwe (1998) argued that this is a typical feature of Barrovian metamorphism and related this feature to the inertia of thermal equilibration. However, Stüwe (1998) also observed that the degree of thermal perturbation (i.e. the departure of peak temperatures from a stable temperature conditions at the depth corresponding to peak pressure) appears to increase along the Eoalpine field gradient with decreasing grade, which is in conflict with models for Barrovian metamorphism (see England and Thompson 1984). The data presented below may shed some light on this debate.

Methods

Two samples from the northern and central Ennstal Complex (EC02, EC05), two samples from the central and southern Wölz Complex (WC22, WC30) and one sample from the central Rappold Complex (RC45) were collected for REE-rich epidote/allanite dating (Fig. 1). These samples were selected from a larger set (94 thin sections, 154 localities) that covers the metamorphic field gradient. We adopt here the distinction between allanite (> 0.5 REE atoms per formula unit (apfu)) and REE-rich epidote (< 0.5 REE apfu) following Gieré and Sorensen (2004). Whole rock major element compositions were acquired via X-ray fluorescence analysis on glass beads with a Bruker Pioneer S4 at the NAWI Graz Geocenter. Trace element compositions were measured at the University of Graz by solution ICP-MS on dissolved powders (Table 1). Further details on analytical conditions and sample preparation can be found in Nong et al. (2022).

A JXA-8530FPlus HyperProbe Electron Probe Micro-analyzer at the NAWI Graz Geocenter was used for mineral compositions and X-ray element mapping. The microprobe is equipped with one energy-dispersive (EDS) and five wavelength-dispersive (WDS) spectrometers. Reference materials and detection limits are given in Table S1. Due to relatively short counting times, the typical 2σ error on Th and U is approximately 5% and 25%, respectively. Th, U and REE-bearing minerals were analyzed with 15 kV acceleration voltage and 150 nA beam current at a beam diameter of 3 μm . Peak overlap corrections were made for Pb-Y, Pb-Th, U-Th, P-Y (Table S2). X-ray element maps were acquired with a focused beam at 15 kV acceleration voltage and 100 nA beam current. X-ray maps for Y, U and Th were measured with WDS, while those for Ce and Zr were measured with EDS. No peak overlap correction was applied for mapping. Maps were processed using XMapTools 4.2 (Lanari et al. 2023). Mineral abbreviations are after Whitney and Evans (2010).

REE-rich epidote/allanite dating

Thin sections from Ennstal Complex samples were prepared perpendicular to the penetrative intersection lineation (Fig. 3) so that mainly basal sections of allanite are exposed (Fig. 4a, b). To get a larger grain surface, both Ennstal Complex samples (EC02, EC05) were crushed to separate additional allanite grains by panning and handheld magnet. Approximately 110 allanite grains per sample were handpicked under a binocular microscope and mounted in epoxy resin. After grinding the mount down to expose the interior of the grains it was polished with a 3 μm and 1 μm diamond paste. Due to their larger grain size, allanite and

Table 1 Bulk rock composition of samples used for allanite and REE-rich epidote dating

Oxides (wt%)	EC02	EC05	WC22	WC30	RC45
SiO ₂	40.41	64.94	51.95	50.72	63.32
TiO ₂	1.66	0.67	0.89	1.29	0.69
Al ₂ O ₃	31.18	17.78	21.84	22.94	17.59
Fe ₂ O ₃ ^{total}	9.46	6.13	9.01	10.44	5.09
MnO	0.06	0.09	0.06	0.14	0.18
MgO	2.63	1.63	4.28	3.18	1.25
CaO	0.15	0.13	0.87	1.22	2.12
Na ₂ O	1.26	1.09	1.77	1.49	2.24
K ₂ O	6.41	3.33	4.31	4.35	3.74
P ₂ O ₅	0.14	0.11	0.23	0.12	0.13
LOI	5.15	2.71	2.98	2.97	2.22
Sum	98.51	98.60	98.20	98.86	98.57
Ca/Ca _{shaw}	0.07	0.06	0.40	0.56	0.97
Al/Al _{shaw}	1.88	1.07	1.31	1.38	1.06
Trace elements ($\mu\text{g/g}$)					
Li	7.6	24.7	33.2	32.7	10.4
Be	1.1	0.8	0.8	0.5	0.5
B	10.0	1.8	1.3	1.2	1.3
Sc	4.9	3.9	7.5	10.5	1.4
V	60.8	27.5	73.7	45.8	9.1
Cr	35.4	27.4	46.1	42.2	7.0
Co	25.4	28.0	31.4	30.8	41.3
Ni	50.8	21.8	45.4	50.8	5.5
Cu	34.8	14.3	29.2	29.2	26.0
Zn	46.7	63.2	138.2	89.4	36.0
Ga	9.6	10.0	12.6	10.0	10.6
Ge	0.7	0.7	0.8	0.9	0.7
As	2.2	25.1	0.9	1.6	2.0
Rb	15.2	36.2	100.2	84.6	24.3
Sr	365.3	22.1	31.6	20.7	34.2
Y	10.1	5.9	15.4	16.4	21.0
Ba	246.1	134.1	279.4	115.6	100.4
La	23.6	24.9	28.5	35.0	47.4
Ce	45.0	52.3	53.3	69.2	90.7
Pr	4.8	5.6	6.3	7.9	9.8
Nd	18.1	20.7	24.0	29.9	32.8
Sm	3.4	3.9	4.6	5.7	5.9
Eu	0.8	0.7	0.9	1.1	0.5
Gd	3.1	3.0	4.0	4.9	5.4
Tb	0.4	0.4	0.5	0.6	0.7
Dy	2.2	1.9	3.0	3.5	4.6
Ho	0.4	0.3	0.6	0.7	0.9
Er	1.1	0.7	1.7	1.9	2.5
Tm	0.1	0.1	0.2	0.3	0.3
Yb	0.9	0.4	1.5	1.8	2.2
Lu	0.1	0.1	0.2	0.3	0.3
Pb	9.4	17.1	5.1	3.6	3.8
Th	5.8	9.8	8.9	11.6	10.4
U	1.4	1.7	2.2	2.0	2.6
Th/U	4.2	5.9	4.1	5.7	4.0

Ca/Ca_{shaw} and Al/Al_{shaw} are the respective Ca and Al contents normalized to the Ca and Al contents from Shaw (1956) and are plotted in Fig. 7b

LOI loss on ignition

REE-rich epidote in samples WC22, WC30 and RC45 could be analyzed directly in thin section. Backscattered electron (BSE) and secondary electron (SE) images were acquired with a JXA-8530F Plus HyperProbe and a Zeiss Gemini DSM982 SEM at the University of Graz (Fig. 5).

The $^{207}\text{Pb}/^{235}\text{U}$, $^{206}\text{Pb}/^{238}\text{U}$ and $^{207}\text{Pb}/^{206}\text{Pb}$ ratios for REE-rich epidote/allanite were determined using a NWR 193 nm ArF Excimer laser coupled to a Nu Plasma II multi-collector (MC)-ICP-MS at the Central Lab for Water, Minerals and Rocks (NAWI Graz Geocenter, Austria). A single

pre-ablation burst with 25 μm diameter was executed before every ablation to remove surface contamination. Ablation was done with a 20 μm spot diameter, 5 Hz repetition rate and a fluence of 2.8 J/cm^2 for 15 s. Sequences of 10 unknown analyses were bracketed by analyses of primary reference materials. Ion-counting detectors (IC) were used to measure ^{202}Hg , ($^{204}\text{Hg} + \text{Pb}$), ^{206}Pb , ^{207}Pb and ^{208}Pb while ^{232}Th and ^{238}U were detected on Faraday cups. A $^{238}\text{U}/^{235}\text{U}$ ratio of 137.818 was used (Hiess et al. 2012). Plešovice zircon (Sláma et al. 2008) was used to standardize $^{207}\text{Pb}/^{235}\text{U}$,

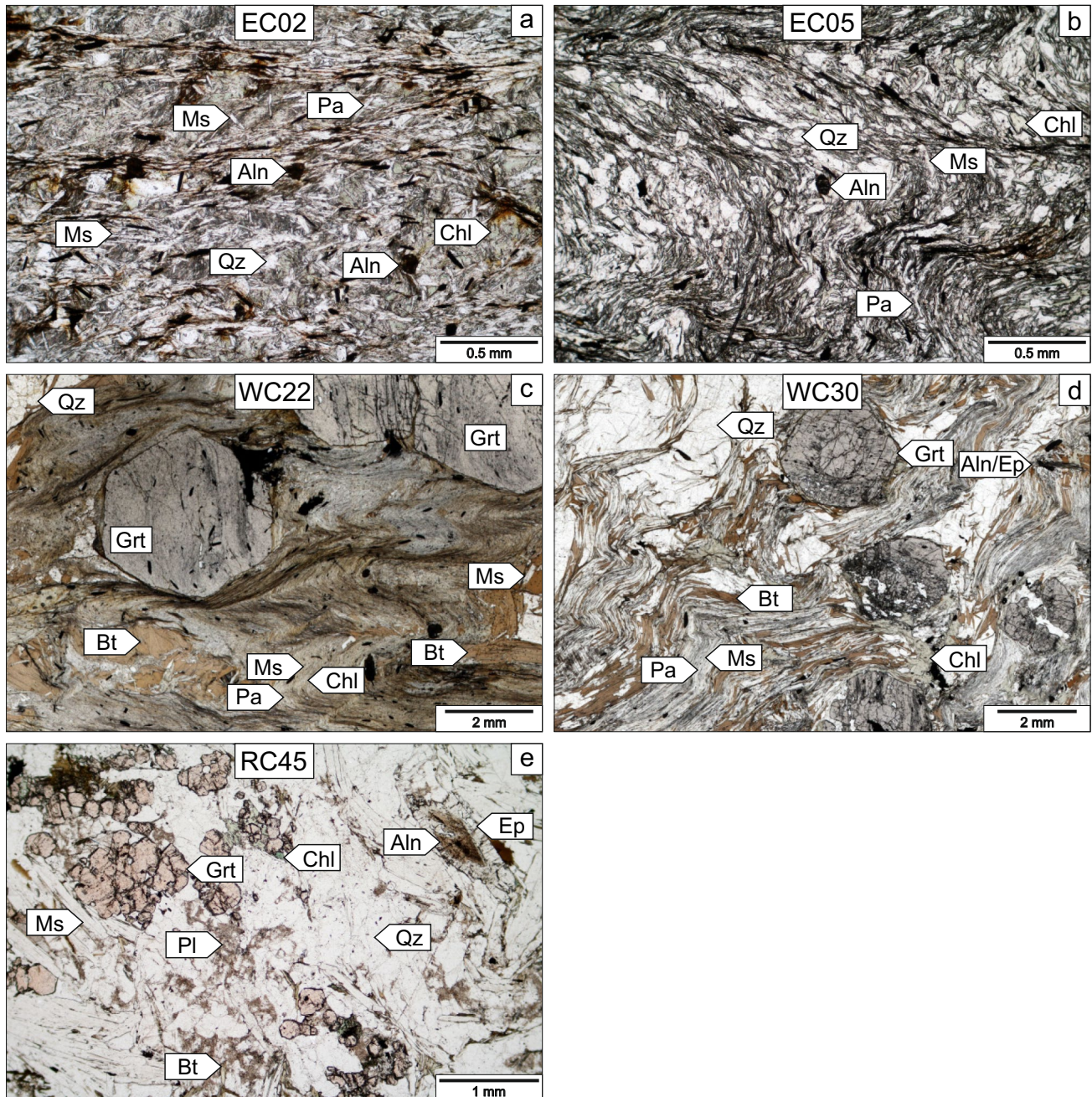


Fig. 3 Representative microphotographs of the rock matrix of sample **a** EC02, **b** EC05, **c** WC22, **d** WC30 and **e** RC45

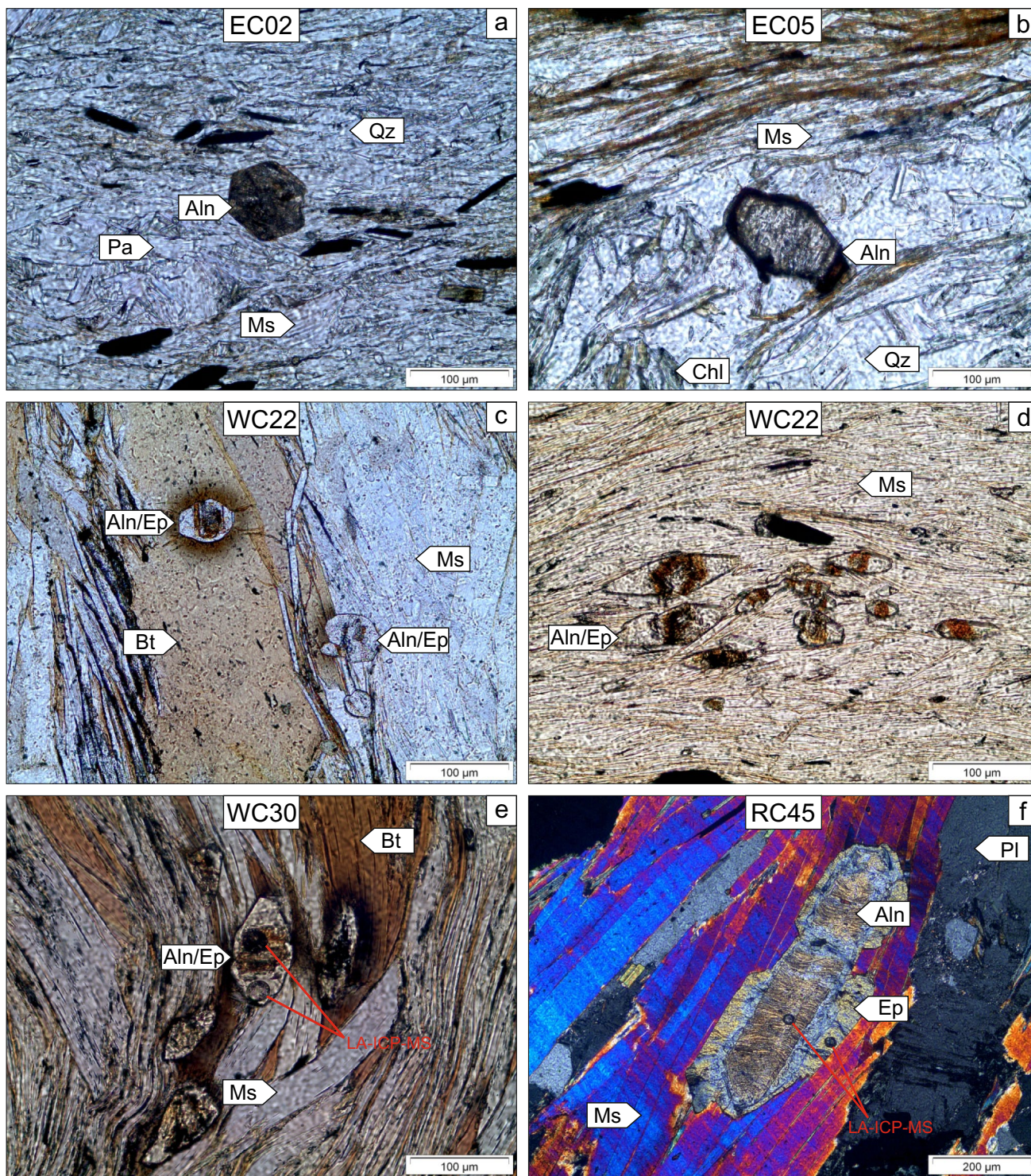


Fig. 4 Representative microphotographs of allanite/REE-rich epidote rims and their textural relations to matrix minerals. **a** Euhedral allanite within the crenulation cleavage (sample EC02). **b** Euhedral allanite in sample EC05. **c** Allanite with REE-rich epidote rims in a biotite blast and within aggregates of biotite and muscovite (sample WC22). **d** Allanite with elongated REE-rich epidote rims in aggregates of fine-grained muscovite within the crenulation cleavage (sam-

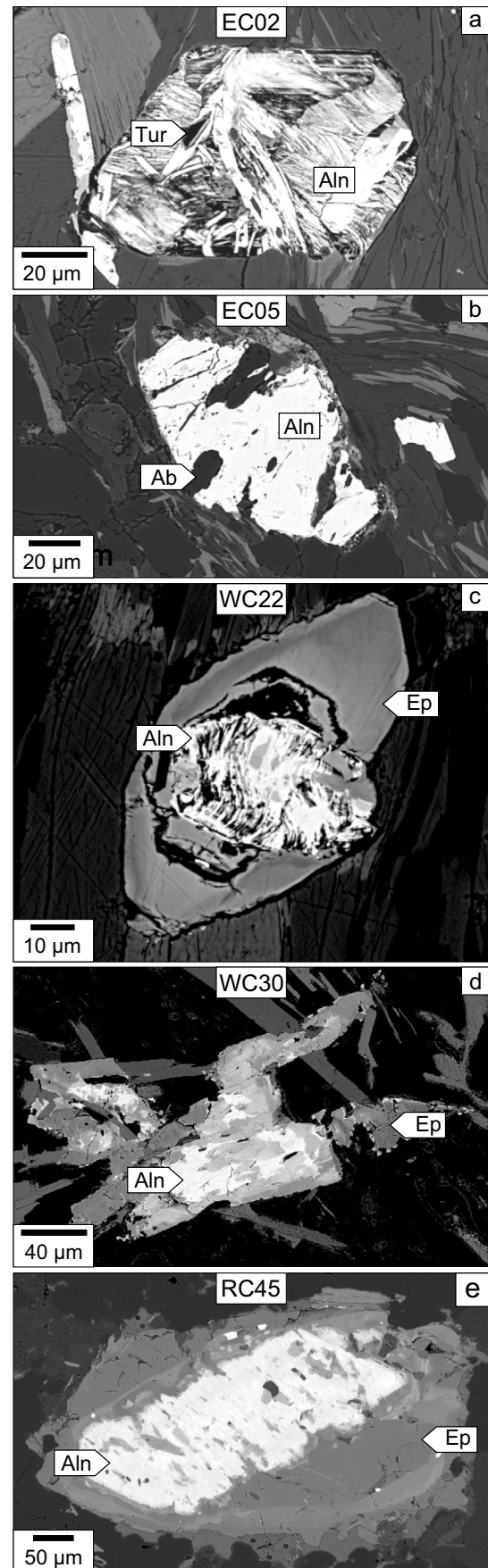
ple WC22). **e** Allanite with elongated REE-rich epidote rims within aggregates of biotite and muscovite in the main foliation (sample WC30). **f** Allanite with a REE-rich epidote rim in a muscovite aggregate (sample RC45) under cross-polarized light. The allanite core appears brown, the inner rim and the enriched domain as grey and the outer rim as yellow

Fig. 5 BSE pictures of allanite and REE-rich epidote. **a** Allanite in sample EC02 displays distinct darker and brighter domains. Note oscillatory zoning in the darker domains. **b** Allanite with albite inclusions is partially surrounded by an incomplete rim (sample EC05). **c** Metamict allanite with a REE-rich epidote rim (sample WC22). A slightly darker middle rim separates the relatively brighter inner and outer rim. **d** Allanite extensively replaced and rimmed by REE-rich epidote (sample WC30). **e** Allanite with a REE-rich epidote rim (sample RC45). The enriched domain separating the inner and outer rim appears as a BSE-bright veil. Within the enriched zone large zircons are visible. The allanite core shows replacement and extensive metamictization

$^{206}\text{Pb}/^{238}\text{U}$ and $^{207}\text{Pb}/^{206}\text{Pb}$ ratios while NIST SRM 612 glass (Pearce et al. 1997) was used for other Pb/Pb ratios. Zircons M257 (Nasdala et al. 2008), 91500 (Wiedenbeck et al. 1995) were used as secondary standards. Secondary reference zircons indicate up to 1.3% accuracy offset on $^{206}\text{Pb}/^{238}\text{U}$ ratios while NIST SRM 612 shows <0.5% accuracy offset on $^{207}\text{Pb}/^{206}\text{Pb}$ ratios. Data reduction was done with Iolite 3.71 (Paton et al. 2011) and the UPbGeochron4 data reduction scheme. IsoplotR ver. 5.0 (Vermeesch 2018) was used to produce Tera-Wasserburg diagrams (Tera and Wasserburg 1972) and regress U–Pb data. Linear regression of U–Pb data yields a lower intercept with the concordia curve regarded as formation date and an intercept with the vertical axis representing the initial $^{207}\text{Pb}/^{206}\text{Pb}$ (Pb_0) composition. An external error of 1.17% was quadratically added to the measured $^{238}\text{U}/^{206}\text{Pb}$ ratios based on the daily variance of secondary reference materials (“excess variance”, Horstwood et al. 2016). This does not affect the lower intercept date and Pb_0 ratio, but lowers the MSWD of the regression. Linear regressions can yield uncertainties on the lower intercept date that are lower than the total analytical uncertainty (signal counting and variance of primary standard analyses, following Iolite’s output) of single data points, which erroneously suggests that the method can resolve differences smaller than the analytical uncertainty. To correct for that, the average uncertainty on $^{238}\text{U}/^{206}\text{Pb}$ ratios in each sample (always greater than that on $^{207}\text{Pb}/^{206}\text{Pb}$ ratios) is quadratically added to the lower intercept date uncertainty (Table 2). These final uncertainties are indicated in brackets after those derived from the linear regression.

Results from secondary reference materials indicate that U–Pb ratios are accurately reproduced for a zircon matrix. Downhole fractionation curves for Plešovice zircon and our allanite samples are similar (<0.1% difference, Fig. S1), indicating an analogous ablation behaviour. This supports the use of a zircon reference material to standardize allanite analyses, provided that only a low crater depth (~5 μm in our case) is used to minimize laser-induced fractionation (e.g., Darling et al. 2012).

Table S3 provides the full list of LA-ICP-MS analytical conditions and Table S4 shows the results of isotopic



analyses. Figures S2–S6 give information on the locations of the measured spots in allanite and REE-rich epidote.

Thermodynamic modelling

Pseudosection modelling of (clino-)zoisite and epidote as proxies for REE-rich epidote was done with *Perple_X* program package (Connolly 2005) and the internally consistent data set *hp622ver.dat* (Holland and Powell 2011) in the MnO-Na₂O-CaO-K₂O-FeO-MgO-Al₂O₃-SiO₂-H₂O (MnNCKFMASH) and MnO-Na₂O-CaO-K₂O-FeO-MgO-Al₂O₃-SiO₂-H₂O-TiO₂-Fe₂O₃ (MnNCKFMASHTO) systems. In the system MnNCKFMASH the activity-composition relationships used are *Fsp(C1)*, *melt(W)*, *Chl(W)*, *Gt(W)*, *Mica(W)*, *Ctd(W)*, *St(W)*, *Bi(W)* and *Crd(W)* (Holland and Powell 2003; White et al. 2014). The activity-composition relationships used in the system MnNCKFMASHTO are *Fsp(C1)*, *melt(W)*, *Chl(W)*, *Gt(W)*, *Mica(W)*, *Ctd(W)*, *St(W)*, *Bi(W)*, *Crd(W)*, *Ilm(WPH)* and *Ep(HP11)* (Holland and Powell 2003, 2011; White et al. 2007, 2014). The equation of state of Sterner and Pitzer (1994) was used for H₂O in both systems and quartz and aqueous fluid were assumed to be in excess.

Petrography and chemistry

Ennstal Complex

Sample EC02 is a phyllite consisting of ≤ 200 μm sized muscovite, paragonite, chlorite and minor amounts of quartz (Fig. 3a). Accessory minerals within the crenulated phyllosilicate layers are allanite, zircon, apatite and rutile with ilmenite rims. Representative chemical analyses of matrix minerals are provided in Table S5. Sample EC02 is relatively poor in CaO (0.15 wt%) and SiO₂ (40.41 wt%) but is enriched in Al₂O₃ (31.18 wt%) and K₂O (6.41 wt%) compared to samples from the Wölz and Rappold Complexes (Fig. 7b; Table 1).

Allanite is euhedral to subhedral in shape with an average diameter of ≤ 100 μm and appears dark brown under transmitted light (Fig. 4a). It can be divided into distinct dark and bright domains on BSE images (Fig. 5a) and locally contains zircon and tourmaline inclusions. The dark domains show oscillatory zoning parallel to the euhedral outline of the grains, whereas the bright domains appear as elongate laths that are randomly oriented within the grain. The dark and bright domains yield similar compositions in most major, minor and trace elements (~ 19 wt% Al₂O₃, ~ 10–11 wt% CaO, ~ 12 wt% FeO, ~ 22 wt% REE₂O₃) although X-ray mapping of Ce distribution shows a lower intensity in the dark domains (Figs. 6a, 7a; Table S6). The largest compositional differences between these domains are in ThO₂ and

P₂O₅ concentrations which are slightly enriched in the dark domains (1.57 wt% ThO₂, 0.76 wt% P₂O₅) relative to the bright domains (0.42 wt% ThO₂, 0.09 wt% P₂O₅).

Sample EC05 from the Ennstal Complex is a phyllite consisting of quartz (≤ 300 μm) layers alternating with crenulated phyllosilicate layers that contain ≤ 200 μm large muscovite, paragonite and chlorite (Fig. 3b). Accessory phases are allanite, zircon, apatite and rutile with ilmenite rims. Representative analyses of matrix minerals are provided in Table S5. Sample EC05 yields a significantly lower CaO (0.13 wt%) bulk-rock concentration compared to samples from the Wölz and Rappold Complexes (Fig. 7b; Table 1).

Allanite appears as dark brown euhedral to subhedral grains with an average diameter of 100 μm within both the phyllosilicate and quartz layers (Fig. 4b). BSE images of allanite show only minor metamictization and albite inclusions (Fig. 5b; Table S5). BSE images and X-ray maps reveal the presence of < 10 μm thick, discontinuous rims around allanite (Figs. 5b, 6b). These rims are enriched in FeO (35.15 wt%), MgO (1.73 wt%), UO₂ (0.18 wt%) and ThO₂ (1.11 wt%) whereas they are depleted in SiO₂ (28.04 wt%), CaO (4.55 wt%) and REE₂O₃ (4.49 wt%) relative to allanite (10.74 wt% FeO, 0.16 wt% MgO, %, < 0.02 wt% UO₂, 0.31 wt% ThO₂, 31.68 wt% SiO₂, 11.69 wt% CaO, 21.65 wt% REE₂O₃) (Table S6).

Wölz Complex

The matrix of micaschist sample WC22 (central Wölz Complex) consists of quartz and crenulated layers of fine-grained muscovite (≤ 200 μm) and paragonite (≤ 200 μm) together with larger biotite (≤ 700 μm) and chlorite (≤ 500 μm) blasts and aggregates (Fig. 3c). Euhedral garnet (up to 5 mm in size) is partly replaced by retrograde chlorite and includes quartz, ilmenite and allanite with REE-rich epidote rims. Garnet zoning reveals a slight increase in *X*_{alm} from 0.57 to 0.67 and *X*_{pyp} from 0.05 to 0.08 from the innermost core to the outermost rim, whereas *X*_{sps} decreases gradually from 0.10 to 0.04. *X*_{grs} is almost constant at 0.24 (Table S7). Albite (< 300 μm) is found in garnet pressure shadows and in microfold hinges where it is partially replaced by paragonite. Accessory minerals are allanite with REE-rich epidote rims and ilmenite. Ilmenite is elongated and oriented parallel to the foliation. Representative analyses of matrix minerals, including a garnet profile, are provided in Tables S5 and S7.

Allanite appears dark brown and subhedral in shape with an average diameter of 30 μm surrounded by 10–50 μm thick REE-rich epidote rims. REE-rich epidote rims are elongated and oriented parallel to the muscovite-biotite layers (Fig. 4c, d). A pleochroic halo surrounds allanite with REE-rich epidote rims that is included in biotite blasts and aggregates. REE-rich epidote rims within garnet are

Table 2 List of samples with information regarding age and chemical composition

Sample	Unit	Domain	Mineral	Avg. Th/U	N	Free regression—Uncorrected ratios			MSWD			
						Age [Ma]	\pm^a [Ma]	\pm prop. ^b [Ma]				
EC02	EC	–	Aln	8.0	16	105.2	3.6	4.0	0.8527	0.0029	3.2	
EC05	EC	–	Aln	18.2	24	279.4	6.3	8.1	0.8619	0.0032	1.6	
WC22	WC	core	Aln	48.6	13	316.4	21.2	22.2	0.8750	0.0240	5.0	
WC30	WC	rim	REE-Ep	2.3	13	98.0	2.3	2.9	0.8430	0.0140	1.1	
WC30	WC	core	Aln	53.4	7	286.2	11.1	12.0	0.8459	0.0096	2.3	
RC45	WC	rim	REE-Ep	3.3	10	96.1	1.7	2.1	0.8468	0.0046	1.4	
RC45	RC	core	Aln	94.0	18	326.9	8.8	11.1	0.8376	0.0010	1.6	
RC45	RC	rim	REE-Ep	0.45	21	101.8	0.9	2.4	0.8262	0.0008	1.7	
Sample	MSWD minimization method— ²³⁰ Th corrected ratios											
	Pr. Th/U	Age [Ma]	\pm^a [Ma]	Age range [Ma]	²⁰⁷ Pb/ ²⁰⁶ Pb ₀	\pm	MSWD					
EC02	0.4	104.9	2.2	102.2–105.4	0.8541	0.0016	3.0					
EC05	1.9	279.4	5.9	272.9–279.5	0.8623	0.0025	1.6					
WC22	0.5	310.8	13.4	298.8–315.9	0.8813	0.0109	3.8					
WC30	0.1	94.3	2.4	93.6–98.1	0.8432	0.0140	0.5					
WC30	∞	–	–	244.1–286.4	–	–	–					
RC45	0.6	95.4	2.3	85.8–96.2	0.8461	0.0046	1.3					
RC45	∞	–	–	161.6–326.0	–	–	–					
RC45	∞	–	–	100.4–101.9	–	–	–					

MSWD mean squared weighted deviation, *N* number of analyses, *EC* Ennstal Complex, *WC* Wölz Complex, *RC* Rappold Complex, *Pr* Predicted

^aUncertainty of regression line in Tera-Wasserburg space

^bTotal age uncertainty taking into account the variance of ²³⁸U/²⁰⁶Pb ratios (see text). All uncertainties are given at 2 σ level

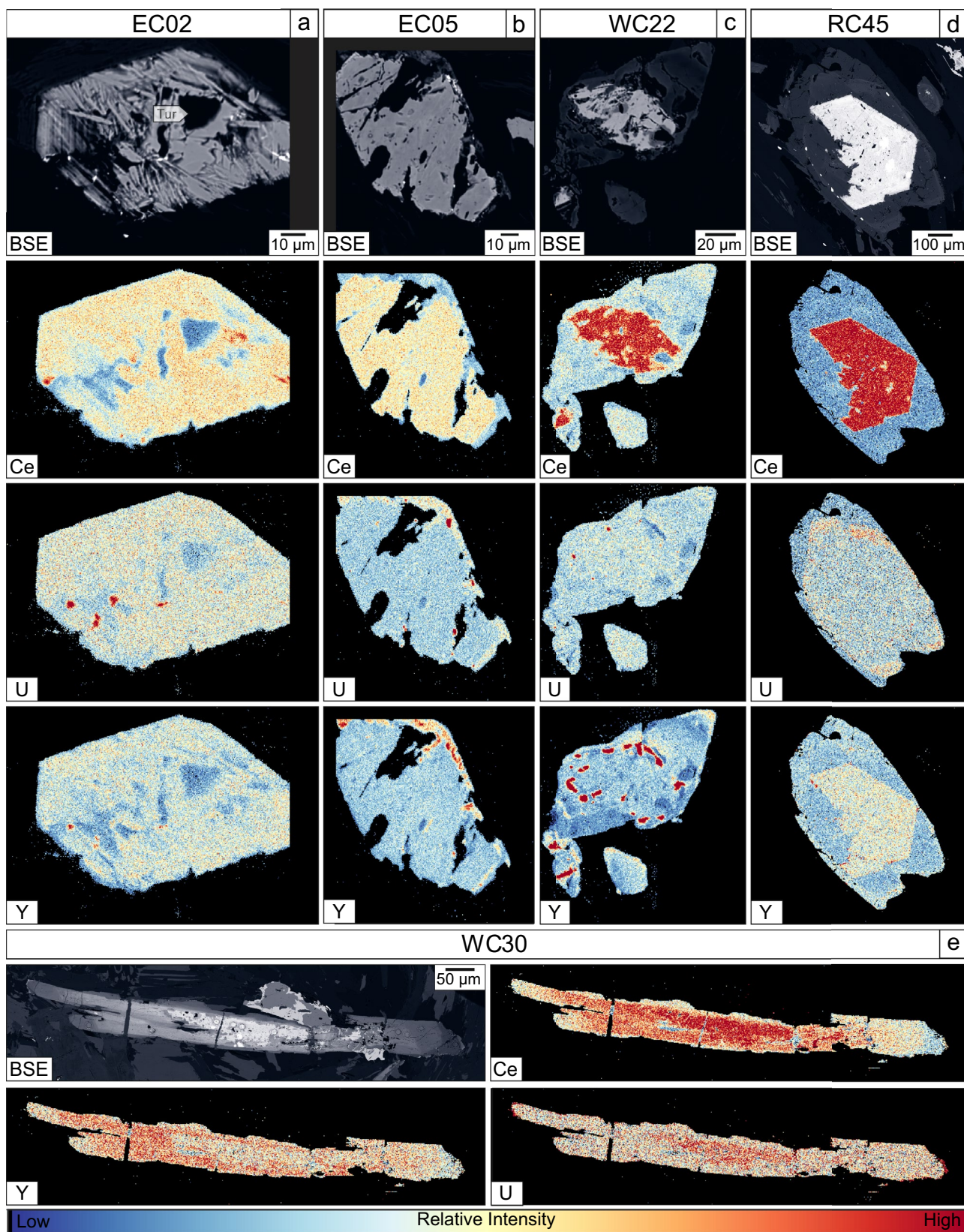


Fig. 6 Wavelength and energy dispersive X-ray maps of selected REE-rich epidote/allanite grains. **a** Sample EC02. **b** Sample EC05. **c** Sample WC22. **d** Sample RC45. **e** Sample WC30. Larger versions of

the same maps and additional element maps can be found in the supplementary material (Figs. S7–S11)

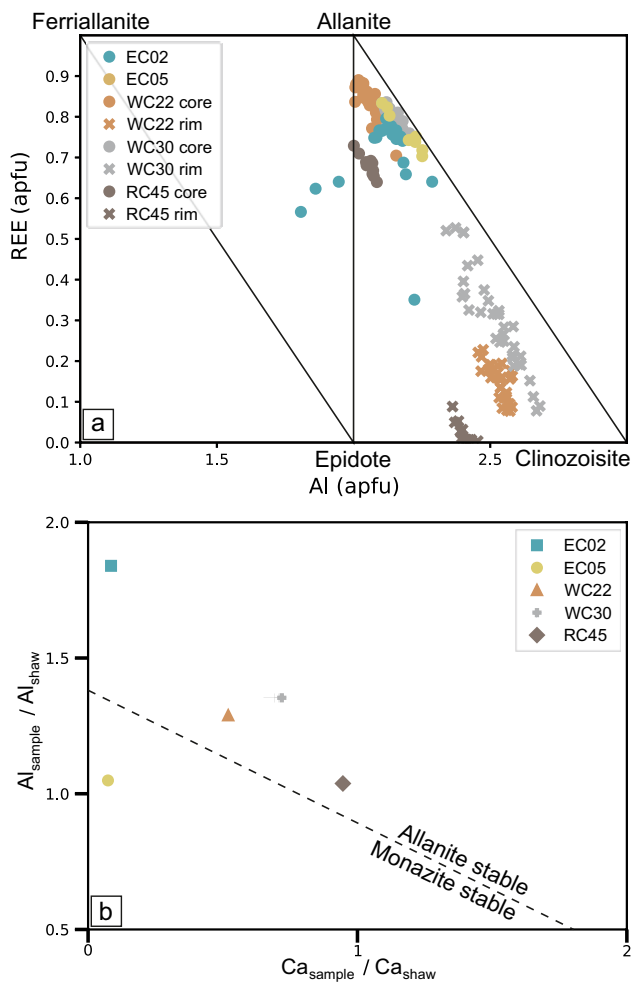


Fig. 7 **a** REE vs. Al diagram after Petřík et al. (1995) showing the composition of allanite and REE-rich epidote in the analysed samples. **b** Bulk rock Ca and Al contents normalized to Shaw's average pelite Ca and Al contents (Table 1). The dashed line separates observed monazite and allanite stability fields for the biotite and garnet zones (Wing et al. 2003)

subhedral or euhedral in shape. BSE images reveal extensive metamictization of the allanite cores and replacement by REE-epidote (Fig. 5c). X-ray maps show an irregular, patchy rim between the allanite core and the REE-rich epidote rim (Fig. 6c), which is enriched in Y. Allanite cores yield the highest REE₂O₃ concentrations (24.36 wt%) while CaO (9.86 wt%) and Al₂O₃ (17.82 wt%) are lower and FeO (12.01 wt%) is higher compared to the rims (Fig. 7a; Table S6). In the REE-rich epidote rims, REEs and Y are decreasing from the innermost rim (5.28 wt% REE₂O₃) to the middle part of the rim (2.34 wt% REE₂O₃). The outermost part ($\leq 10 \mu\text{m}$) of the rim is again enriched in REE₂O₃ (6.13 wt%). FeO and CaO concentrations at the rim are approximately 7 and 20 wt%, respectively. Al₂O₃ slightly decreases from the innermost to the outermost rim (27.06–25.59 wt%).

Sample WC30 from the southern Wölz Complex exhibits a matrix of quartz, muscovite, paragonite, biotite, garnet, plagioclase, chlorite and allanite with REE-rich epidote rims (Fig. 3d). Rutile, ilmenite, apatite and zircon are accessory phases. The main foliation is defined by microfolded muscovite ($\leq 1 \text{ mm}$), paragonite ($\leq 800 \mu\text{m}$) and biotite ($\leq 2 \text{ mm}$) layers. Garnet is approximately 1.5 mm wide with $\leq 1 \text{ mm}$ thick rims. The core-rim transition is characterized by numerous quartz inclusions. Chlorite partially replaces garnet. Apatite, zircon and rutile with ilmenite rims are visible as inclusions within garnet. Garnet zoning shows an increase in X_{alm} and X_{pyp} from 0.60 to 0.75 and 0.05 to 0.15 from inner to outer core, respectively. In the same portion of the garnet, X_{grs} slightly decreases from 0.10 to 0.06. At the core-rim transition, X_{alm} and X_{pyp} drop to 0.62 and 0.06, respectively, while X_{grs} increases from 0.06 to 0.25. From inner to outer rim X_{alm} and X_{pyp} increase to 0.7 and 0.07 whereas X_{grs} slightly decreases to 0.21. X_{sps} displays a gradual decrease from innermost core (0.23) to outermost rim (0.05) (Table S8). Relics of plagioclase ($< 1 \text{ mm}$) are found in garnet pressure shadows and in microfold hinges where they are partially replaced by muscovite and paragonite. Rutile with ilmenite rims are oriented parallel to the main foliation. Representative analyses of matrix minerals and a garnet profile are provided in Tables S5 and S8.

The $\leq 500 \mu\text{m}$ anhedral allanite cores are surrounded and partly replaced by $\leq 800 \mu\text{m}$ thick subhedral or anhedral REE-rich epidote rims. REE-rich epidote rims within muscovite and biotite aggregates in the foliation appear as pressure shadows and are oriented parallel to the foliation (Fig. 4e). Allanite with REE-rich epidote rims is also included in garnet rims. Allanite shows minor metamictization and some grains show extensive replacement by REE-rich epidote (similar to “mosaic allanite” described by Boston et al. 2017) (Fig. 5d). These replacement zones yield lower REE concentrations (18.5 wt% REE₂O₃) than the allanite cores (23.8 wt% REE₂O₃). The REE-rich epidote rims yield lower and decreasing REE concentrations from the inner rim to the outer rim (10.1 to 2.4 wt% REE₂O₃) (Fig. 6e). ThO₂ is enriched in the replacement zone (1.05 wt%) compared to the allanite core (0.58–0.80 wt%) and the innermost and outermost rim (0.58 and < 0.03 wt%). CaO and FeO are increasing and decreasing, respectively, from the allanite core (10.93 wt% CaO, 10.65 wt% FeO) to the outermost REE-rich epidote rim (22.31 wt% CaO, 4.88 wt% FeO). Al₂O₃ follows the same trend as CaO and increases from the allanite core (18.6 wt%) towards the outer rim (28.99 wt%) (Fig. 7a; Table S6).

Rappold Complex

Sample RC45 from the central Rappold Complex contains quartz, muscovite, biotite, plagioclase, chlorite, garnet and

allanite with REE-rich epidote rims (Fig. 3e). Accessory minerals are zircon, apatite, sulfides, calcite, rutile and ilmenite. The main foliation is crenulated and is formed by muscovite aggregates and blasts (≤ 1 mm), biotite (≤ 200 μm) and chlorite (≤ 100 μm). Plagioclase (≤ 500 μm) shows strong sericitic alteration. Anhedral garnet is ≤ 1.2 mm in size and contains zircon inclusions. Highly variable X_{alm} , X_{pyr} , X_{grs} and X_{sp} show no clear increasing or decreasing trend from core to rim (Table S9). Biotite and Fe-Ti-rich chlorite locally surround garnet and fill cracks therein. Allanite with REE-rich epidote rims are included within large muscovite aggregates (Fig. 4f). Representative analyses of matrix minerals and a garnet profile are provided in Tables S5 and S9. The bulk composition of sample RC45 is enriched in CaO (2.12 wt%) compared to all other samples (Fig. 7b; Table 1).

Euhedral to subhedral allanite reaches up to 700 μm in size and is surrounded by ≤ 500 μm thick REE-rich epidote rims (Figs. 4f, 5e). Allanite cores show pervasive metamictization and partial replacement by REE-rich epidote. The REE-rich epidote rims can be divided into an inner and an outer rim separated by an enriched domain (Fig. 5e, 6d). The inner rim yields REE and Y concentrations below detection limit. The enriched domain yields higher REE₂O₃ (2.77 wt%), ThO₂ (0.33 wt%) and UO₂ (0.30 wt%) concentrations compared to the outer (0.63 wt% REE₂O₃, 0.04 wt% ThO₂, 0.80 wt% UO₂) and inner rim (<0.03 wt% ThO₂, 0.03 wt% UO₂). Overall, the rim yields higher CaO (20–23 wt%) and lower FeO concentrations (9–10 wt%) compared to the allanite core (12.01 wt% CaO, 12.02 wt% FeO). Al₂O₃ is higher at the rim (25–27 wt%) than the core (18–19 wt%) (Table S6). Discontinuous trails of tiny zircon grains (<20 μm) are common in the matrix where they cut across garnet porphyroblasts. Allanite cores also yield tiny zircon trails (Figs. S16, S17). Tiny zircons are included in the inner rim whereas larger zircons (≤ 20 μm) are included in the enriched domain and are oriented parallel to it (Figs. 5e, 6d). The outer rim has no zircon inclusions.

REE-rich epidote and allanite dating results

Ennstal Complex

For the Ennstal Complex, 28 spots on 23 allanite grains and 29 spots on 29 grains were measured in sample EC02 and EC05, respectively. In sample EC02, 12 analyses from the BSE dark domains show significant scatter and are not regressed (Fig. 8a). Sixteen spots from the BSE bright domains define a discordia with a lower intercept date of 105.2 ± 3.6 (4.0) Ma and a MSWD of 3.2. The intercept of

the discordia with the vertical axis indicates an initial lead composition ($^{207}\text{Pb}/^{206}\text{Pb}_0$) of 0.8527 ± 0.0029 (Fig. 8f).

For sample EC05, five obvious outliers were discarded while the remaining 24 analyses define a lower intercept date of 279.4 ± 6.3 (8.1) Ma (MSWD = 1.6) and an initial $^{207}\text{Pb}/^{206}\text{Pb}_0$ ratio of 0.8619 ± 0.0032 (Fig. 8b, f).

Wölz Complex

In sample WC22, 22 spots on 22 allanite cores were analyzed. Nine outlier analyses from metamict parts were discarded while the remaining 13 analyses define a discordia with a lower intercept date of 316.4 ± 21.2 (22.2) Ma (MSWD = 5) and an initial $^{207}\text{Pb}/^{206}\text{Pb}_0$ ratio of 0.8750 ± 0.0240 (Fig. 8c, f). Thirteen analyses from the REE-rich epidote rims define a discordia with a lower intercept date of 98.0 ± 2.3 (2.9) Ma (MSWD = 1.1) and an initial $^{207}\text{Pb}/^{206}\text{Pb}_0$ ratio of 0.8430 ± 0.0014 (Fig. 8c, f). Due to the size of REE-rich epidote rims, the laser spots overlapped the innermost, middle and outermost parts.

For sample WC30, 19 spots on 11 allanite cores and 16 spots on six epidote rims were measured. For the allanite cores 12 outliers were discarded as they display higher $^{238}\text{U}/^{206}\text{Pb}$ ratios ascribed to partial lead loss (Fig. 8d). Seven remaining analyses define a discordia with a lower intercept date of 286.2 ± 11.1 (12.0) Ma (MSWD = 2.3) and an initial $^{207}\text{Pb}/^{206}\text{Pb}_0$ ratio of 0.8459 ± 0.0096 . For REE-rich epidote rim, six analyses from the replacement zone were discarded (Fig. 8d) and the remaining 10 analyses from the inner and outer rim give a lower intercept date of 96.1 ± 1.7 (2.1) Ma (MSWD = 1.4) and an initial $^{207}\text{Pb}/^{206}\text{Pb}_0$ ratio of 0.8468 ± 0.0046 .

Rappold Complex

For sample RC45, 28 spots on 10 allanite cores were measured. 10 analyses were discarded as they display partial lead loss or were measured in metamict parts (Fig. 8e). The remaining 18 allanite analyses define a discordia with a lower intercept date of 326.9 ± 8.8 (11.1) Ma (MSWD = 1.6) and an initial $^{207}\text{Pb}/^{206}\text{Pb}_0$ ratio of 0.8376 ± 0.001 . Of 22 analyses from nine REE-rich epidote rims only one outlier measured in the inner rim was discarded. The remaining 21 analyses come from the enriched domain and the outer rim. Analyses from the outer rim yield a lower intercept date of 102.0 ± 6.5 Ma (MSWD 1.6), while those from the enriched domain give 95.3 ± 3.5 Ma (MSWD = 0.8) (Figs. S12, S13). Because these results are statistically indistinguishable, outer rim and enriched domains analyses were pooled to calculate a discordia with a lower intercept date of 101.8 ± 0.9 (2.4) Ma (MSWD = 1.7) and an initial $^{207}\text{Pb}/^{206}\text{Pb}_0$ ratio of 0.8262 ± 0.0008 (Fig. 8e, f).

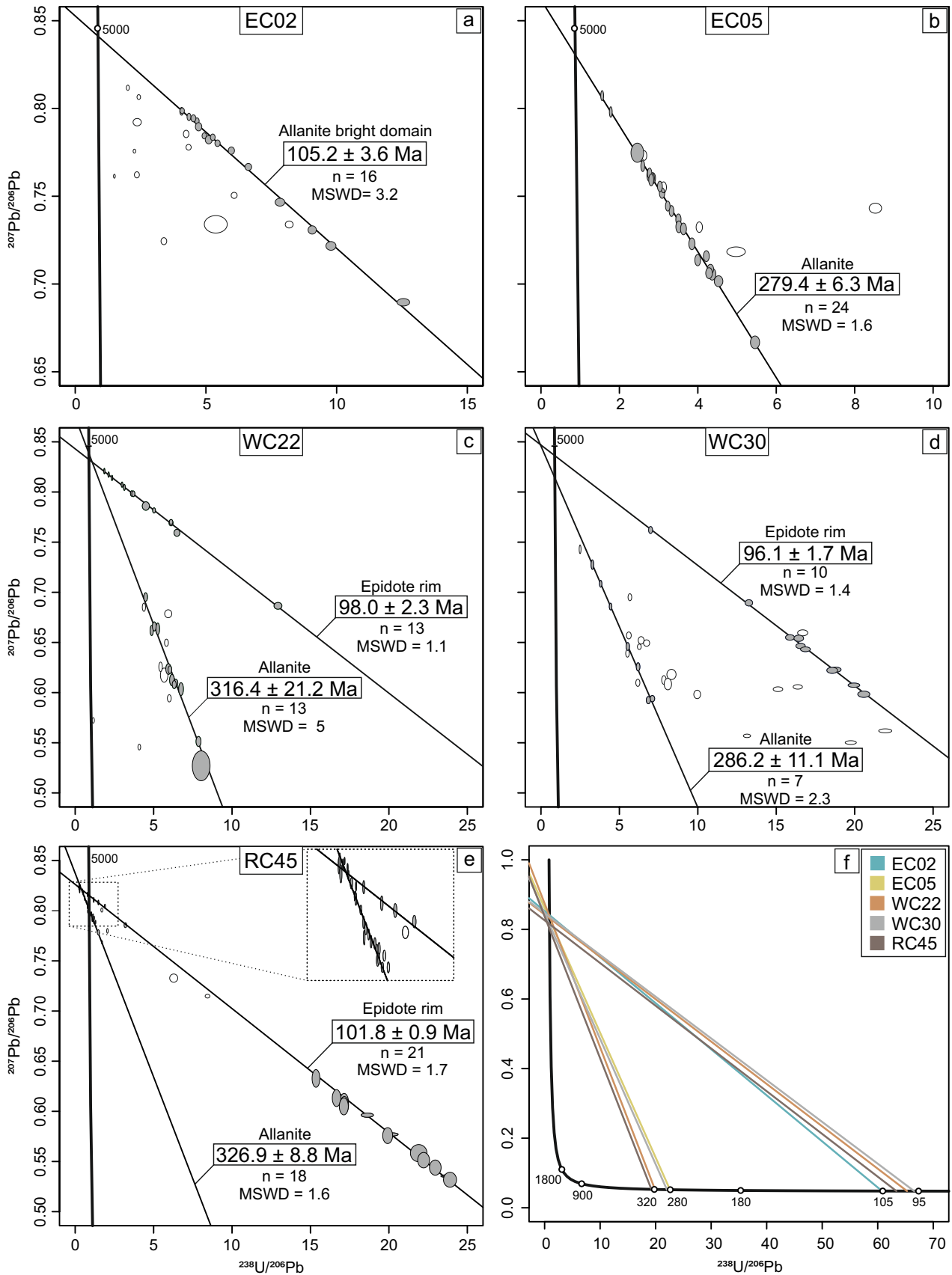


Fig. 8 Tera-Wasserburg diagrams for U–Pb analyses of allanite and REE-rich epidote rims. Discarded analyses are depicted as open ellipses. Grey ellipses were used for regression. Thick black line represents the concordia. The dates provided in the figure are derived from the lower intercept. **a** Sample EC02. Discarded analyses with lower $^{238}\text{U}/^{206}\text{Pb}$ ratios were mostly obtained in BSE darker domains. **b** Sample EC02. **c** Sample WC22. The large scatter of core analyses is due to the small grain size and extensive metamictization **d** Sample WC30. Discarded analyses from the replacement zone plot in between the two regressed discordias. **e** Sample RC45. Analyses from the enriched zone of the rim yield $^{238}\text{U}/^{206}\text{Pb}$ ratios between 15 and 25. Analyses from the outer rim yield $^{238}\text{U}/^{206}\text{Pb}$ ratios between 0 and 5. The inset is a zoomed-in section with outer rim and allanite core analyses. **f** Summary of linear regressions for all samples

^{230}Th disequilibrium correction

A potential issue with U–Pb dating of Th-rich minerals is that they incorporate more ^{230}Th , an intermediate product from the $^{238}\text{U}/^{206}\text{Pb}$ decay chain, than that in secular equilibrium with ^{238}U in the reservoir they grow from. For magmatic samples, Schärer (1984) proposed a way to correct for this disequilibrium by comparing the Th/U ratio in the dated mineral with that in the sample, assuming that the whole rock analysis reflects the composition of the magma at the time of crystallization. This approach is hard to envisage in metamorphic rocks, even less when several generations of REE-rich epidote/allanite are identified. Instead we introduce a new method based on minimizing the MSWD value of the regression. It is primarily devised to evaluate the effect of potential ^{230}Th disequilibrium on lower intercept date and $^{207}\text{Pb}/^{206}\text{Pb}_0$ results. Provided that the MSWD is significantly improved, the method can possibly approximate the Th/U ratio of the reservoir and use it for correction.

Our strategy relies on discarding the lowest possible amount of spot analyses, unless textural (crack, metamictization, inclusion) or analytical (irregular signals, U/Pb fractionation strongly different from that of the reference material) arguments are available. This usually removes clear outliers that often derive from metamict domains, and leaves a set of ‘valid’ data with some scatter (MSWD > 1). This scatter can result from the combined effects of geological processes (growth timing, alteration) and ^{230}Th disequilibrium. Because LA-ICP-MS cannot resolve age differences smaller than ~3% (e.g. Klötzli et al. 2009), and altered domains are assumed to be excluded from ‘valid’ analyses, only the contribution of ^{230}Th disequilibrium remains to be tested. For all ‘valid’ data points, the method iteratively corrects the measured $^{238}\text{U}/^{206}\text{Pb}$ and $^{207}\text{Pb}/^{206}\text{Pb}$ ratios with different values of $(\text{Th}/\text{U})_{\text{reservoir}}$ and regresses the corrected ratios in Tera-Wasserburg space.

The main idea is that a given $(\text{Th}/\text{U})_{\text{reservoir}}$ value will improve the topology of data points to a point where their scatter reflects analytical errors only (MSWD approaches

unity; Wendt and Carl 1991). This is potentially achievable because the magnitude of the ^{230}Th disequilibrium correction depends on the Th/U ratio of individual analyses (Parrish 1990; Snye et al. 2014). It requires the assumption that all analyzed domains formed out of a reservoir with a homogeneous Th/U ratio, which is not necessarily the case at low-grade conditions. For example, Skrzypek et al. (2018) propose that the composition of monazite formed above ~600 °C reflects cm-scale equilibration, whereas large Th/U variations are preserved at lower temperature as a result of local equilibria. Different $(\text{Th}/\text{U})_{\text{reservoir}}$ ratios for different cogenetic domains can, however, cancel out or drastically enhance the effect of ^{230}Th disequilibrium, so that the MSWD of the regression cannot be improved through our approach. The improvement of the MSWD value should therefore be critically evaluated. If significant, the hypothesis of a single $(\text{Th}/\text{U})_{\text{reservoir}}$ value and its use for correction might be considered valid. Any remaining scatter is due to our wish to discard as few spots as possible, and is very likely caused by undetected alteration (metamictization, recrystallization).

A first case is illustrated by allanite core analyses of sample WC22. The method is able to significantly reduce the MSWD of regression (3.8 instead of 5.0) as well as uncertainties on lower intercept date (4.3% instead of 6.7%) and $^{207}\text{Pb}/^{206}\text{Pb}_0$ ratio (1.2% instead of 2.7%), with a central age of 310.8 Ma that could be more robust. It, however, shows that the central age might vary by about 5% (298.8–315.9 Ma) and that the data point scatter remains high (3.8). The latter likely reflects the presence of metamict domains among regressed spot analyses, which is a common feature of allanite in this sample.

A second case is shown by sample EC02, for which a minimum MSWD of 3.0 (instead of 3.2) is reached for a $(\text{Th}/\text{U})_{\text{reservoir}}$ of 0.4, which yields a lower intercept date (104.9 ± 2.2 Ma) and a $^{207}\text{Pb}/^{206}\text{Pb}_0$ ratio (0.8541 ± 0.0016) indistinguishable within uncertainty from results obtained with uncorrected data (Figs. 8a, 9). This, together with the fact that the lower intercept date will only vary between 102.2 and 105.4 (for possible $(\text{Th}/\text{U})_{\text{reservoir}}$ values from 0.05 to 10), suggests that a ^{230}Th -disequilibrium correction will not significantly influence age accuracy and geological interpretation. The results for other samples are given in Table 2. For core analyses in WC30 and RC45, the dates obtained with uncorrected data are only approached at extreme $(\text{Th}/\text{U})_{\text{reservoir}}$ values, suggesting growth in a strongly Th-enriched environment (e.g. after monazite). In general, no significant improvement of the MSWD was achieved, so that no ^{230}Th -disequilibrium correction was actually applied to our data. The method served here primarily to assess potential age variations.

Thermodynamic modelling of (clino-)zoisite and epidote stability

REE-free vs. REE-bearing systems

Several attempts have been made to model the stability of REE-bearing phases (e.g. Spear 2010; Janots et al. 2007, Hoschek 2016) using models for dissakisite and allanite. We first evaluate the influence of REE on the modelled stability of epidote-group minerals by comparing the modelling results in REE-bearing systems of Hoschek (2016) and Janots et al. (2007) with those from REE-free systems.

For that, we model (clino-)zoisite and epidote stabilities using the bulk compositions of Janots et al. (2007) and Hoschek (2016), normalized to 100 wt% (sample A of Hoschek 2016) in the REE-free systems MnNCKFMASH and MnNCKFMASHTO (Fig. 10a). We consider these samples to be not very oxidized; 10% of the total Fe was assumed to be Fe₂O₃ and was included in the MnNCKFMASHTO system and effectively removed for the MnNCKFMASH system. In the MnNCKFMASH system, both zoisite and clinozoisite can be modelled as pure phases. Clinozoisite is the stable phase at lower temperature (< 390 °C) whereas orthorhombic zoisite is stable above 390 °C (Fig. 10). The stability field displayed in this system is a combination of the stability fields of clinozoisite and zoisite.

The modelled (clino-)zoisite fields extend from 345 °C/0.2 GPa to 530–560 °C and > 1.5 GPa (Fig. 10a). The epidote field extends from 280 °C/< 0.1 GPa to 550 °C and > 1.5 GPa and is slightly wider than the REE-rich epidote/allanite or dissakisite stability fields modelled in

REE-bearing systems (Janots et al. 2007; Hoschek 2016) (Fig. 10a). The fields become slightly wider with increasing bulk Ca, Al and Fe³⁺ contents, similar to REE-rich epidote (Hoschek 2016). Overall, the stability fields of epidote-group minerals modelled in REE-free and REE-bearing systems have very similar boundaries in *P–T* space, showing that modelling results with currently available activity-composition models for REE-phases do not significantly differ from those obtained in REE-free systems.

Modelling the investigated samples

In view of the fact that the stability fields of epidote-group minerals appear to be similar in the REE-free and REE-bearing systems, we now model the stability of (clino-)zoisite and epidote for our own bulk compositions in the MnNCKFMASH and MnNCKFMASHTO systems, respectively. The measured bulk composition (Table 1) of the samples investigated was normalized to 100 wt% and 10% of the total Fe was assumed to be Fe₂O₃. Modelling results with an effective bulk composition considering element fractionation in garnet cores (sample WC30) and Ca fractionation in accessory calcite (0.25 mode% in sample RC45) do not yield significant differences in epidote-group mineral stabilities. Pseudosections in the range of 200–600/700 °C and 0.1–2 GPa were calculated for samples WC22, WC30 and RC45. Modelling results for sample WC30, considered representative in terms of major oxide concentrations and pseudosection topology, are shown in Fig. 10 with the stability fields of (clino-)zoisite (MnNCKFMASH) and epidote (MnNCKFMASHTO) highlighted. The same pseudosections are displayed in Figs. S14 and S15 with all fields labeled. (Clino-)zoisite in samples WC22 and WC30 is stable from 310–320 °C/0.1–0.2 GPa to 550 °C/1.4–1.5 GPa while epidote stability extends from 225 °C/< 0.1 GPa to 575 °C/1.6–1.8 GPa. In sample RC45, (clino-)zoisite is stable from 320 °C/0.1 GPa to 625 °C/1.4 GPa. Epidote is stable from < 200 °C/< 0.1 GPa to 675 °C/1.7 GPa.

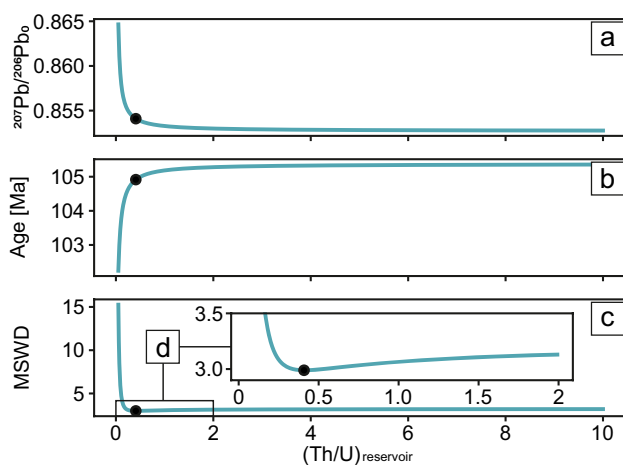


Fig. 9 Diagrams showing theoretical changes in **a** initial lead composition, **b** age and **c** MSWD for allanite analyses in sample EC02 as a function of Th disequilibrium correction for different Th/U_{reservoir} ratios. **d** Inset shows that the minimum of the MSWD curve is attained at (Th/U)_{reservoir} ≈ 0.4

Discussion

Modelling the stability and growth of REE-rich epidote

It was shown above, that the stability fields of epidote-group minerals modelled in REE-free and REE-bearing systems are very similar (Fig. 10a). (Clino-)zoisite stability in the MnNCKFMASH system thus provides a plausible minimum *P–T* range in which epidote-group minerals are expected to be stable (Fig. 11). Conversely, the epidote stability field obtained in the MnNCKFMASHTO system is wider, and slightly larger than that of REE-bearing epidote

Fig. 10 Pseudosection modelling results **a** Comparison of the stability fields of REE-bearing and REE-free epidote-group minerals of the same bulk compositions from Janots et al. (2007) and Hoschek (2016). Pseudosections for Sample WC30 highlighting the stability fields of (clino-)zoisite (blue line) and epidote (red line) in the **b** MnNCKFMASH system and **c** MnNCKFMASHTO system, respectively. Thick blue line depicts the stability of (clino-)zoisite as a combination of Czo and Zo. The top left inset shows the respective bulk composition used for calculating the pseudosections. Main fields are labelled (see Figs. S14 & S15 for all field labels). Fields: 1. Chl Ms Ab Wrk, 2. Chl Ms Ab Hul, 3. Ms Chl Stp Ab Hul, 4. Ms Pg Chl Stp Ab Hul, 5. Ms Pg Chl Pmp Stp Ab, 6. Ms Pg Chl Czo Stp Ab, 7. Ms Pg Chl Czo Ab, 8. Ms Pg Chl Pmp Ab, 9. Ms Pg Chl Grt Pmp Ab, 10. Ms Pg Grt Chl Lws Pmp, 11. Ms Pg Chl Grt Zo, 12. Ms Pg Chl Bt Grt Zo, 13. Ms Pg Grt Chl Bt Zo Ab, 14. Ms Chl Grt Zo Ab, 15. Chl Ms Bt Grt Zo Ab, 16. Grt Chl Ms Pg Bt Pl, 17. Bt Pl Chl Grt Ms Zo, 18. Chl Pl Bt Ms, 19. Pl Chl Ms Bt Ab, 20. Pl Chl Ms Bt Ab. **(b)** Pseudosection in the MnNCKFMASHTO system. Thick red line depicts the stability field of epidote. Fields: 1. Ms Pg Chl Spn Ab Hul, 2. Ms Pg Chl Spn Stp Ab Hul, 3. Chl Ms Pg Lws Spn Stp Ab, 4. Ms Pg Chl Lws Spn Stp, 5. Ep Ms Pg Chl Spn Stp Ab, 6. Ms Pg Chl Ep Spn Stp, 7. Chl Ms Pg Lws Spn, 8. Chl Ep Ms Pg Spn, 9. Chl Ms Pg Lws Spn Rt, 10. Ep Chl Ms Pg Spn Rt, 11. Chl Ms Pg Lws Spn Rbk Rt, 12. Ms Pg Chl Grt Lws Spn Rb Rt, 13. Ms Pg Chl Grt Lws Rbk Rt, 14. Ms Pg Chl Grt Lws Rt Acm, 15. Ep Chl Ms Pg Grt Spn Rt, 16. Ms Pg Chl Grt Ep Rt, 17. Ms Pg Grt Chl Rt, 18. Grt Ms Pg Chl Bt Rt, 19. Grt Chl Bt Ms Pg Ilm Rt, 20. Grt Ms Pg Ilm Bt Chl, 21. Pl Ilm Grt Chl Bt Ms, 22. Chl Bt Pl Ilm Ms, 23. Pl Ms Bt Chl Ilm Ab, 24. Ep Chl Ms Spn Ab, 25. Ms Pg Chl Ep Spn Ab

in REE-bearing systems (Janots et al. 2007; Hoschek 2016), so that it can be regarded as the maximum stability range for epidote-group minerals. In both REE-free and REE-bearing systems, the stability field of epidote-group minerals is bounded by breakdown reactions involving Ca-bearing, major minerals like zeolites, lawsonite or plagioclase (Figs. 10, S14, S15; see also Janots et al. 2007). It is very likely the limited P - T dependence of these reactions that explains the similarity between modelled epidote and allanite stabilities.

Constraining the P - T conditions of REE-epidote growth and resorption during metamorphism is more challenging. A peculiar feature of modelled stability fields is the concentric shape of modal isopleths (e.g. Hoschek 2016); the modal amount of epidote increases towards the center of the stability field. For any prograde path, this predicts REE-epidote growth only in the low-temperature half of the stability field. (Clino-)zoisite, epidote and allanite fields are all centered at about 450 °C, which coincides well with the first appearance of allanite at ~400–450 °C reported for numerous natural samples (Janots et al. 2006, 2007, 2008; Goswami-Banerjee and Robyr 2015). Along a prograde metamorphic path, the centre of the modelled fields (~450 °C) provides the maximum temperature of REE-rich epidote growth. The epidote stability field is wider than the (clino-)zoisite stability field due to the addition of Fe^{3+} and yields a lower P - T boundary (~225 °C/ $<$ 0.5 GPa instead of 325 °C/ $<$ 0.6 GPa) for the growth of REE-rich epidote along a prograde path.

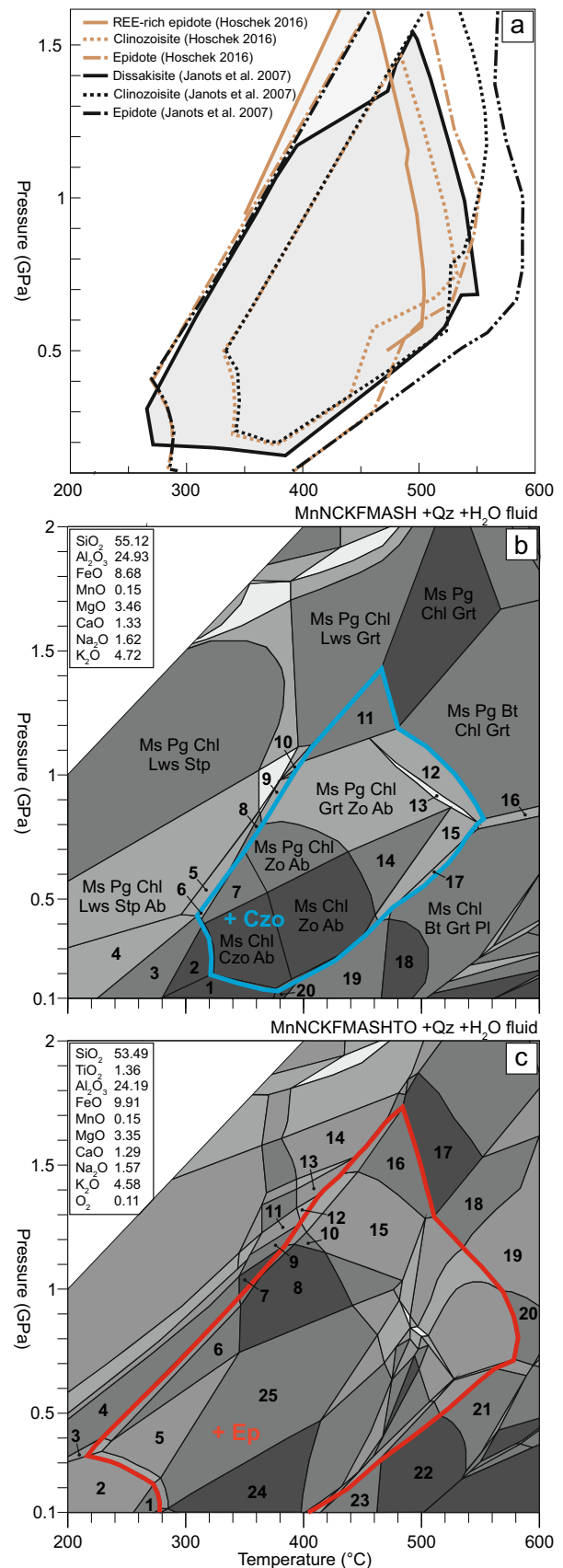


Fig. 11 Pseudosections of **a** sample WC22 **b** WC30 and **c** RC45 ▶ highlighting the stability fields of epidote (dash-dotted) and (clino-)zoisite (dashed). Metamorphic gradients depicted with a solid line are from Faryad and Hoinkes (2003). Metamorphic gradients depicted with a dashed line are drawn using P - T estimates of incipient garnet growth (depicted as open rectangles) from Gaidies et al. (2006). The blue areas constrained by the epidote-in, the allanite-in and the metamorphic gradients are interpreted as the P - T ranges for prograde REE-rich epidote growth. Dashed Grt-in lines are modelled in the MnNCKFMASH system, dash-dotted Grt-in lines are modelled in the MnNCKMFASHTO system. No bulk composition correction for Mn fractionation in garnet was done. Garnet-in lines therefore represent the minimum P - T conditions of incipient garnet growth

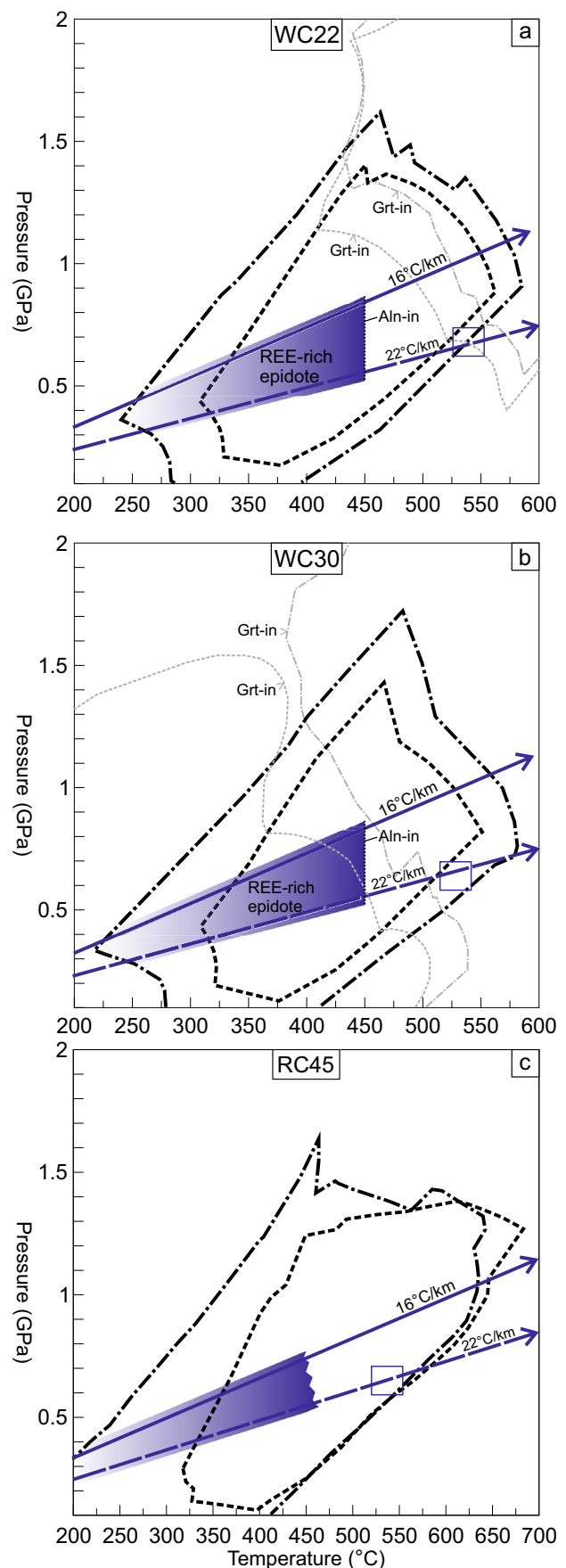
To obtain the P - T conditions of REE-rich epidote growth in our samples, we use a similar approach to Goswami-Banerjee and Robyr (2015). We combine geothermal gradients with modelling results of the stability fields of the end-members (clino-)zoisite/epidote (Fig. 11a, b). For both samples WC22 and WC30, maximum P - T conditions for the appearance of REE-rich epidote lie at approximately 450 °C and 0.8 GPa. The minimum P - T estimates for samples WC22 and WC30 are 250 °C/0.3 GPa and 225 °C/0.2 GPa, respectively (Fig. 11a, b). Although epidote can occur at such low P - T conditions, these estimates should be regarded with caution as equilibrium is only attained at a millimeter scale or lower (Ruiz Cruz et al. 2010).

Sample RC45 differs from those in the Wölz Complex. Although the REE-rich epidote rims also appear elongated and are included in large muscovite aggregates oriented parallel to the foliation, they do not yield gradually decreasing REE concentrations (Figs. 4f, 6d). In fact, the inner rim yields REE concentrations below detection limit while the enriched zone and the outer rim show almost constant REE contents. We interpret this as a sign of REE-rich epidote growth due to the influx of a fluid rather than progressive metamorphism. Since REEs mostly reside in Variscan allanite cores, REE-epidote growth during the Eoalpine event takes place in a virtually REE-free system, as indicated by the rather low REE content of the rims (Fig. 7a; Table S6). Nevertheless, considering a similar gradient as for the Wölz Complex and the relatively high modal abundance of epidote, the possible P - T range in which the fluid infiltrated is constrained at 200–450 °C and 0.25–0.8 GPa.

P - T conditions and timing of allanite/REE-rich epidote growth

Ennstal Complex

In the Ennstal Complex, additional samples that are not shown in this study contain euhedral allanite included in large biotite blasts around which the main Eoalpine foliation is deflected (Stumpf 2023). This is interpreted as Permian allanite formation before or at the same time as biotite,



during prograde metamorphism (279.4 ± 8.1 Ma). The P – T conditions of Permian metamorphism were higher than those of the Eoalpine overprint (Iglseider et al. 2022), which is responsible for the present-day, low-grade appearance of the Ennstal Complex. Contemporaneous Permian metamorphism in the Ennstal Complex and Koralpe-Wölz nappe system indicates a similar mid-crustal position for all units during that period. The absence of biotite and garnet in both dated samples from the Ennstal Complex further supports that peak metamorphic temperatures of 490–565 °C were reached during the Permian cycle and were never exceeded during the Eoalpine overprint at 105.2 ± 4.0 Ma (Iglseider et al. 2022). No peak pressure estimations are available for the Ennstal Complex. We propose that pressure during the Eoalpine overprint was lower than 0.8 GPa based on the lower greenschist facies paragenesis and assuming the Ennstal Complex entered the Eoalpine subduction zone along a similar gradient as the adjacent units from the Koralpe-Wölz nappe system. This implies that the growth of BSE-bright laths inside former, euhedral allanite (Fig. 5a) occurred at P – T conditions lower than 490–565 °C and 0.8 GPa, close to the metamorphic peak in the lower greenschist facies (Froitzheim et al. 2008).

Samples EC02 and EC05 reacted differently to the Eoalpine overprint. Allanite in sample EC05 remained largely unaffected except for the appearance of small discontinuous rims (Fig. 6b). These rims are the only indicator of allanite alteration; they are thought to reflect allanite breakdown and the formation of a subsequent phase (tiny monazite is found in other Ennstal Complex samples) during low-grade Eoalpine overprint. On the other hand, the internal texture of allanite in sample EC02 was significantly changed. Thin BSE-bright allanite laths formed at the expense of former (Permian?) allanite. This difference very likely reflects the contrast in bulk rock compositions. The relatively low Ca and Al contents of sample EC05 limit epidote stability and an alteration to monazite is expected (Fig. 7b). Conversely, the high Al content of sample EC02 fostered (REE-bearing) epidote growth after allanite.

Wölz Complex

The Permian age in sample WC30 (286.2 ± 12.0 Ma) is slightly older but in line with previous Th–U–Pb monazite ages of 261 ± 18 Ma and 267 ± 9 Ma in the Koralpe-Wölz nappe system (Krenn et al. 2012; Schulz 2017). However, no textural information is available to constrain Permian allanite growth due to the pervasive Eoalpine overprint. Nonetheless, we interpret the significant size and euhedral shape of allanite cores to be an indication of prograde growth rather than retrograde replacement of a former REE-rich phase like monazite. The age obtained from allanite cores in sample WC22 (316.4 ± 22.2 Ma) overlaps within error

with the Permian age from sample WC30 (286.2 ± 12.0 Ma) as well as with the Variscan age from sample RC45 (326.9 ± 11.1 Ma). Extensive metamictization and a small grain size is the most likely explanation for this large uncertainty and this date is deemed inconclusive.

In both samples from the Wölz Complex, REE-rich epidote rims appear as elongated pressure shadows around allanite. They are oriented parallel to the main, variably microfolded foliation in samples WC22 and WC30 (Fig. 4c, d, e). Allanite with REE-rich epidote rims is included in garnet (Eoalpine garnet and two-phase garnet rim), muscovite, paragonite and biotite aggregates and blasts. Decreasing REE contents from the inner to the outer rim are interpreted as element fractionation during prograde growth. These textures indicate prograde REE-rich epidote crystallization (98.0 ± 2.9 Ma, 96.1 ± 2.1 Ma) during formation of the main foliation. This likely occurred in a deformation stage at the onset of Eoalpine metamorphism, preceding metamorphic peak pressure. Incipient Eoalpine garnet growth in the Wölz Complex is estimated at 540–570 °C and 0.6–0.8 GPa (Gaidies et al. 2006; Bestel et al. 2009). This further constrains the crystallization of the REE-rich epidote rims, which is in agreement with our modelled maximum P – T conditions of 450 °C and 0.8 GPa.

Rappold Complex

No textural information to constrain Variscan allanite growth (326.9 ± 11.1 Ma) is available in sample RC45. Due to the large size and euhedral shape of allanite cores, we also ascribe them to prograde growth rather than retrograde replacement. The Variscan age matches the mid-Carboniferous Th–U–Pb monazite and Lu–Hf garnet-whole-rock metamorphic ages of 335–310 Ma reported in other units of the Koralpe-Wölz nappe system (Krenn et al. 2012; Schulz 2017; Hauke et al. 2019). This further supports the hypothesis of Variscan garnet growth in the Rappold Complex (Gaidies et al. 2006, 2008).

Since it is not possible to temporally resolve the different growth domains in the epidote rims, we suggest that rim crystallization happened in a relatively short time span due to influx of a fluid. Furthermore, the age of 101.8 ± 2.4 Ma and the fact that the REE-rich rims are included in muscovite forming the crenulated foliation points to REE-rich epidote rim crystallization during a prograde deformational stage of Eoalpine metamorphism at comparable P – T conditions as REE-rich epidote rim crystallization in samples WC22 and WC30. Micro-zircon trails similar to those found in RC45 were reported as inclusions in chloritoid from low-grade schist in the Eastern Alps (Hollinetz et al. 2022) (Fig. S16). In this case, a formation through Zr-saturated fluid at greenschist facies conditions (< 500 °C) is inferred. We

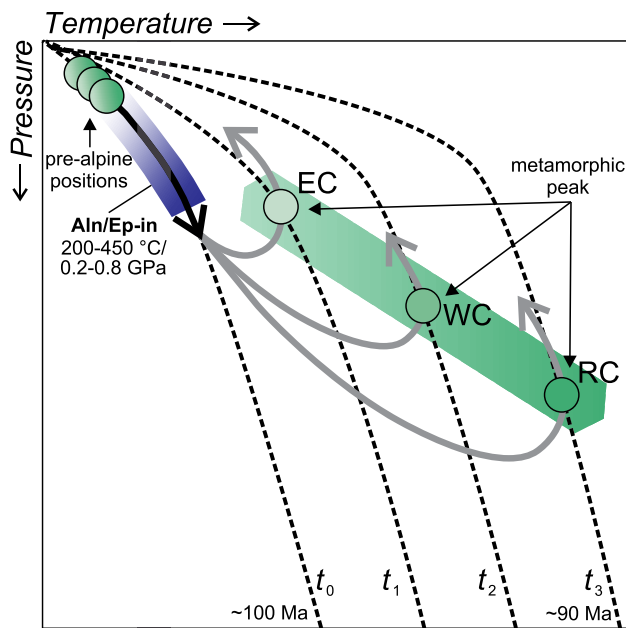


Fig. 12 Schematic P - T diagram illustrating the Eoalpine P - T - t evolution of the investigated units. The blue area indicates REE-rich epidote/allanite appearance along the prograde path. The black arrow shows the P - T path broadly shared by all units while the grey arrows show the subsequent P - T evolution of individual units. Dashed lines are geotherms at different time steps (t_0 , t_1 ,...). The green domain is the exposed metamorphic field gradient

consider this as further evidence for the formation of REE-rich epidote rims at greenschist facies conditions.

Tectonic implications

There are no Eoalpine ages for the Ennstal, Wölz and Rappold Complex to directly compare our dating results to. We therefore compare our data to dating results from the high-grade eclogite facies part of the Koralpe-Wölz nappe system to give an estimation on the duration of the Eoalpine cycle. The ages of sample EC02 (105.2 ± 4.0 Ma), WC22 (98.0 ± 2.9 Ma), WC30 (96.1 ± 2.1 Ma) and RC45 (101.8 ± 2.4 Ma) are older or slightly overlap with the ages of initial garnet growth at 95–94 Ma but are considerably older than the ages of the subsequent metamorphic pressure peak at 90–88 Ma (Thöni et al. 2008). This suggests a time span of 6–15 My for prograde metamorphism of the studied units from 0.2 to 1.1 GPa (Faryad and Hoinkes 2003).

For the Eoalpine event, the difference between P - T conditions of REE-rich epidote/allanite appearance and peak P - T conditions varies between units. Peak metamorphic temperature in the Ennstal Complex is constrained to less than 490–565 °C (Iglseider et al. 2022), suggesting that partial allanite recrystallization during Eoalpine overprint occurred relatively close to the peak. In the southern part of

the Wölz Complex, peak Eoalpine conditions of 600–650 °C and 1–1.1 GPa were reached, although they decrease towards the north (Faryad and Hoinkes 2003; Froitzheim et al. 2008). The difference between REE-rich epidote rim crystallization at maximum 450 °C and 0.8 GPa and peak conditions is therefore larger than in the Ennstal Complex. In the Rappold Complex, similar peak conditions of 600–650 °C and 1.0–1.1 GPa in the northern part have been documented, but they increase towards the south (Faryad and Hoinkes 2003; Froitzheim et al. 2008). Here, the difference between prograde REE-rich epidote rim growth and peak conditions is even more substantial.

Dating in all units along the field gradient yields similar results of ~100 Ma, indicating that REE-rich epidote/allanite growth conditions during the Eoalpine P - T - t evolution were all reached roughly at the same time. Conversely, the age of peak P - T conditions becomes younger with increasing metamorphic grade (Thöni et al. 2008). This diachronous character of peak metamorphic ages has been formerly interpreted in terms of a southward propagation of units that were incorporated into the subduction channel at different times (Schuster et al. 2013).

However, our results indicate that all units entered the continental subduction channel nearly at the same time. We therefore argue that diachronous peak metamorphic ages simply result from the inertia of thermal equilibration (England and Richardson 1977). For all units, the onset of burial is associated with a nearly instantaneous pressure increase without much heating of the geotherm, which leads to broadly similar REE-rich epidote/allanite ages during heating and burial along the geothermal gradient (t_0) shown on Fig. 12.

Low-grade metamorphic rocks at shallow crustal depth (Ennstal Complex in our case) will reach their metamorphic peak early, begin their exhumation and cool down. As such, they preserve a unique record of the geothermal gradient related to the early stages of continental subduction. Conversely, rocks buried to greater depths have a significantly longer time to equilibrate before their proximity to the surface initiates cooling, so that their metamorphic peak is reached later. This interpretation supports the applicability of the classic models for Barrovian metamorphism to the Eoalpine metamorphic evolution (see also Stüwe 1998). An implication of this interpretation is that there is no need to invoke tectonic processes at different times for rocks of different metamorphic grades.

Conclusions

REE-rich epidote and allanite geochronology for different units (Ennstal Complex, Wölz Complex, Rappold Complex) of a metamorphic field gradient exposed in the

Eastern Alps reveals the timing of Variscan (Carboniferous), Permian and Eoalpine (Cretaceous) events. The effect of ^{230}Th disequilibrium on dating results was evaluated with a new method based on minimizing the MSWD value of regressed U–Pb data. This approach might offer the possibility to approximate the Th/U ratio of the reservoir out of which allanite/REE-rich epidote grew, which can then be used for correction.

In the Ennstal and Wölz Complexes, allanite yields Permian ages of 279.4 ± 8.1 Ma and 286.2 ± 12.0 Ma, respectively. Allanite in the Rappold Complex yields a Variscan age of 326.9 ± 11.1 Ma. REE-rich epidote rims from the Wölz (98.0 ± 2.9 Ma, 96.1 ± 2.1 Ma) and Rappold Complexes (101.8 ± 2.4 Ma) and BSE-bright laths in allanite of one sample from the Ennstal Complex (105.2 ± 4.0 Ma) all yield Eoalpine ages of ~ 100 Ma.

Textural relations between REE-rich epidote rims and muscovite, biotite or garnet show that the former crystallized during an early deformational stage of prograde Eoalpine metamorphism. Additionally, we show that the modelled stability of epidote-group minerals in REE-free and REE-bearing systems is nearly identical. Pseudosection modelling in the REE-free systems MnNCKFMASH and MnNCKFMASHTO combined with geothermal gradients and textures constrain a P – T range of incipient REE-rich epidote growth of 200–450 °C and 0.2–0.8 GPa.

All investigated units entered the Eoalpine subduction channel nearly at the same time, independent of their peak metamorphic grade. The subsequent P – T evolution of each unit towards the metamorphic peak did not necessarily involve differently timed tectonic processes but could simply reflect the inertia of thermal equilibration.

Supplementary Information The online version contains supplementary material available at <https://doi.org/10.1007/s00410-024-02130-3>.

Acknowledgements Sharp comments from two anonymous reviewers and editorial handling by Dante Canil greatly helped to improve the manuscript. S. Schorn and K. Karner-Rühl are thanked for fruitful discussions. C. Iglseder and R. Schuster from Geosphere Austria are thanked for consultation regarding field work and regional geology. C. Hauenberger is thanked for providing access to NAWI Graz facilities. The help of D. Gallhofer for LA-ICP-MS dating is greatly acknowledged. B. Huet is thanked for stimulating discussions on allanite stability. T. Pettke is thanked for supporting the finalization of this paper.

Funding Open access funding provided by University of Graz.

Declarations

Conflict of interest The authors have no relevant financial or non-financial interests to disclose.

Open Access This article is licensed under a Creative Commons Attribution 4.0 International License, which permits use, sharing, adaptation, distribution and reproduction in any medium or format, as long as you give appropriate credit to the original author(s) and the source, provide a link to the Creative Commons licence, and indicate if changes

were made. The images or other third party material in this article are included in the article's Creative Commons licence, unless indicated otherwise in a credit line to the material. If material is not included in the article's Creative Commons licence and your intended use is not permitted by statutory regulation or exceeds the permitted use, you will need to obtain permission directly from the copyright holder. To view a copy of this licence, visit <http://creativecommons.org/licenses/by/4.0/>.

References

- Airaghi L, Janots E, Lanari P, de Sigoyer J, Magnin V (2019) Allanite petrochronology in fresh and retrogressed garnet-biotite metapelites from the Longmen Shan (Eastern Tibet). *J Petrol* 60:151–176. <https://doi.org/10.1093/ptrology/egy109>
- Bestel M, Gawronski T, Abart R, Rhede D (2009) Compositional zoning of garnet porphyroblasts from the polymetamorphic Wölz Complex, Eastern Alps. *Mineral Petrol* 97:173–188. <https://doi.org/10.1007/s00710-009-0084-z>
- Boston KR, Rubatto D, Hermann J, Enig M, Amelin Y (2017) Geochronology of accessory allanite and monazite in the Barrovian metamorphic sequence of the Central Alps, Switzerland. *Lithos* 286–287:502–518. <https://doi.org/10.1016/j.lithos.2017.06.025>
- Chang R, Neubauer F, Liu Y, Genser J, Guan Q, Huang Q, Yuan S (2023) Permian to Triassic protolith ages of type locality eclogites in the Eastern Alps: implications for the opening of the Meliata back-arc basin. *Geology* 51:537–542. <https://doi.org/10.1130/G50903.1>
- Connolly JAD (2005) Computation of phase equilibria by linear programming: a tool for geodynamic modeling and its application to subduction zone decarbonation. *Earth Planet Sci Lett* 236:524–541. <https://doi.org/10.1016/j.epsl.2005.04.033>
- Darling JR, Storey CD, Engi M (2012) Allanite U–Th–Pb geochronology by laser ablation ICPMS. *Chem Geol* 292–293:103–105. <https://doi.org/10.1016/j.chemgeo.2011.11.012>
- England PC, Richardson SW (1977) The influence of erosion upon the mineral fades of rocks from different metamorphic environments. *J Geol Soc* 134:201–213. <https://doi.org/10.1144/gsjgs.134.2.0201>
- England PC, Thompson A (1984) Pressure-temperature-time paths of regional metamorphism I. Heat transfer during the evolution of regions of thickened continental crust. *J Petrol* 25:894–928. <https://doi.org/10.1093/ptrology/25.4.894>
- Faryad SW, Hoinkes G (2003) P – T gradient of Eo-Alpine metamorphism within the Austroalpine basement units east of the Tauern Window (Austria). *Mineral Petrol* 77:129–159. <https://doi.org/10.1007/s00710-002-0196-1>
- Faupl P, Wagerich M (1996) Basin analysis of the Gosau Group of the northern Calcareous Alps (Turonian-Eocene, eastern Alps). In: Welley G and Liebl W (ed) Oil and gas in Alpidic Thrust Belts and Basins of Central and Eastern Europe, vol 5. EAGE Special Publication, London, pp 127–135
- Foster G, Parrish RR, Horstwood MSA, Chenery S, Pyle J, Gibson HD (2004) The generation of prograde P–T-t points and paths; a textural, compositional, and chronological study of metamorphic monazite. *Earth Planet Sci Lett* 228:125–142. <https://doi.org/10.1016/j.epsl.2004.09.024>
- Froitzheim N, Plasienska D, Schuster R (2008) Alpine tectonics of the Alps and Western Carpathians. In: McCann T (ed) The Geology of Central Europe Volume 2: Mesozoic and Cenozoic, 1st edn. Geological Society of London, London, pp 1141–1232. <https://doi.org/10.1144/CEV2P6>
- Gaidies F, Abart R, De Capitani C, Schuster R, Connolly JAD, Reusser E (2006) Characterization of polymetamorphism in the Austroalpine basement east of the Tauern Window using garnet isopleth

- thermobarometry. *J Metamorph Geol* 24:451–475. <https://doi.org/10.1111/j.1525-1314.2006.00648.x>
- Gaidies F, Krenn E, De Capitani C, Abart R (2008) Coupling forward modelling of garnet growth with monazite geochronology: an application to the Rappold Complex (Austroalpine crystalline basement). *J Metamorph Geol* 26:775–793. <https://doi.org/10.1111/j.1525-1314.2008.00787.x>
- Gasser D, Rubatto D, Bruand E, Stüwe K (2012a) Large-scale, short-lived metamorphism, deformation, and magmatism in the Chugach metamorphic complex, southern Alaska: a SHRIMP U-Pb study of zircons. *Geol Soc Am Bull* 124:886–905. <https://doi.org/10.1130/B30507.1>
- Gasser D, Bruand E, Rubatto D, Stüwe K (2012b) The behaviour of monazite from greenschist facies phyllites to anatectic gneisses: an example from the Chugach Metamorphic Complex, southern Alaska. *Lithos* 134–135:108–122. <https://doi.org/10.1016/j.lithos.2011.12.003>
- Gieré R, Sorensen SS (2004) Allanite and other REE-rich epidote-group minerals. *Rev Mineral Geochem* 56:431–493. <https://doi.org/10.2138/gsrmg.56.1.431>
- Goswami-Banerjee S, Robyr M (2015) Pressure and temperature conditions for crystallization of metamorphic allanite and monazite in metapelites: a case study from the Miyar Valley (high Himalayan Crystalline of Zaskar, NW India). *J Metamorph Geol* 33:535–556. <https://doi.org/10.1111/jmg.12133>
- Gregory CJ, Rubatto D, Allen CM, Williams IS, Hermann J, Ireland T (2007) Allanite micro-geochronology: A LA-ICP-MS and SHRIMP U-Th-Pb study. *Chem Geol* 245:162–182. <https://doi.org/10.1016/j.chemgeo.2007.07.029>
- Hauke M, Froitzheim N, Nagel TJ, Miladinova I, Fassmer K, Fonseca ROC, Sprung P, Münker C (2019) Two high-pressure metamorphic events, Variscan and Alpine, dated by Lu-Hf in an eclogite complex of the Austroalpine nappes (Schobergruppe, Austria). *Int J Earth Sci* 108:1317–1331. <https://doi.org/10.1007/s00531-019-01708-8>
- Heaman L, Parrish RR (1991) U-Pb geochronology of accessory minerals. In: Heaman L, Ludden J (eds) Applications of radiogenic isotope systems to problems in geology. Mineralogical Association of Canada, Short-course Handbook, vol 19, pp 59–102
- Hejl E (1997) ‘Cold spots’ during the Cenozoic evolution of the Eastern Alps: thermochronological interpretation of apatite fission-track data. *Tectonophysics* 272:159–173. [https://doi.org/10.1016/S0040-1951\(96\)00256-9](https://doi.org/10.1016/S0040-1951(96)00256-9)
- Hetherington CJ, Dumond G (2013) Versatile monazite: resolving geological records and solving challenges in materials science. *Am Mineral* 98:81–818. <https://doi.org/10.2138/am.2013.4454>
- Hiess J, Condon DJ, McLean N, Noble SR (2012) $^{238}\text{U}/^{235}\text{U}$ Systematics in terrestrial uranium-bearing minerals. *Sci* 355:1610–1614. <https://doi.org/10.1126/science.1215507>
- Holland T, Powell R (2003) Activity-composition relations for phases in petrological calculations: an asymmetric multicomponent formulation. *Contrib Mineral Petrol* 145:492–501. <https://doi.org/10.1007/s00410-003-0464-z>
- Holland T, Powell R (2011) An improved and extended internally consistent thermodynamic dataset for phases of petrological interest, involving a new equation of state for solids. *J Metamorph Geol* 29:333–383. <https://doi.org/10.1111/j.1525-1314.2010.00923.x>
- Hollinetz MS, Schneider DA, McFarlane CRM, Huet B, Rantitsch B, Grasemann B (2022) Bulk inclusion micro-zircon U-Pb geochronology: a new tool to date low-grade metamorphism. *J Metamorph Geol* 40:207–227. <https://doi.org/10.1111/jmg.12624>
- Horstwood MSA, Košler J, Gehrels G et al (2016) Community-derived standards for LA-ICP-MS U-(Th-)Pb geochronology—uncertainty propagation, age interpretation and data reporting. *Geostand Geoanal Res* 40:311–332. <https://doi.org/10.1111/j.1751-908X.2016.00379.x>
- Hoscheck G (2016) Phase relations of the REE minerals florencite, allanite and monazite in quartzitic granet-kyanite schist of the Eclogite Zone, Tauern Window, Austria. *Eur J Mineral* 28:735–750. <https://doi.org/10.1127/ejm/2016/0028-2549>
- Iglseder C, Rantitsch G, Stumpf S, Skrzypek E, Schuster R, Huet B (2022) An adapted tectonic model for the “Central and Eastern Greywacke Zone”—new geochronological and RSCM-data (Styria/Austria). *Ber Geol Bundesanst* 143:83
- Janots E, Negro F, Brunet F, Goffé B, Engi M, Bouybauouéne ML (2006) Evolution of the REE mineralogy in HP-LT metapelites of the Sebtime complex, Rif, Morocco: monazite stability and geochronology. *Lithos* 87:214–234. <https://doi.org/10.1016/j.lithos.2005.06.008>
- Janots E, Brunet F, Goffé B, Poinssot C, Burchard M, Cemič L (2007) Thermochemistry of monazite-(La) and dissakisite-(La): implications for monazite and allanite stability in metapelites. *Contrib Mineral Petrol* 154:1–14. <https://doi.org/10.1007/s00410-006-0176-2>
- Janots E, Engi M, Berger A, Allaz J, Schwarz JO, Spandler C (2008) Prograde metamorphic sequence of REE minerals in pelitic rocks of the Central Alps: implications for allanite-monazite-xenotime phase relations from 250 to 610 °C. *J Metamorph Geol* 26:509–526. <https://doi.org/10.1111/j.1525-1314.2008.00774.x>
- Janots E, Engi M, Rubatto D, Berger A, Gregory C, Meinert R (2009) Metamorphic rates in collisional orogeny from in situ allanite and monazite dating. *Geology* 37:11–14. <https://doi.org/10.1130/G25192A.1>
- Klötzli U, Klötzli E, Zekeriya G, Kosler J (2009) Accuracy of laser ablation U-Pb zircon dating: results from a test using five different reference zircons. *Geostand Geoanal Res* 33:5–15. <https://doi.org/10.1111/j.1751-908X.2009.00921.x>
- Knoll T, Schuster R, Huet B, Mali H, Onuk P, Horschinegg M, Ertl A, Giester G (2018) Spodumene pegmatites and related leucogranites from the AustroAlpine Unit (Eastern Alps, Central Europe): field relations, petrography, geochemistry, and geochronology. *Can Mineral* 56:489–528. <https://doi.org/10.3749/canmin.1700092>
- Krenn E, Schulz B, Finger F (2012) Three generations of monazite in Austroalpine basement rocks to the south of the Tauern Window: evidence for Variscan, Permian and Eo-Alpine metamorphic events. *Swiss J Geosci* 105:343–360. <https://doi.org/10.1007/s00015-012-0104-6>
- Kroner U, Romer RL (2013) Two plates—many subduction zones: the Variscan orogeny reconsidered. *Gondwana Res* 24:298–329. <https://doi.org/10.1016/j.gr.2013.03.001>
- Lanari P, Markmann T, Laughton J, Tedeschi M (2023) XMapTools 4.2 (v.4.2). Zenodo. <https://doi.org/10.5281/zenodo.8058640>
- Nasdala L, Hofmeister W, Norberg N et al (2008) Zircon M257—a homogeneous natural reference material for the ion microprobe U-Pb analysis of zircon. *Geostand Geoanal Res* 32:247–265. <https://doi.org/10.1111/j.1751-908X.2008.00914.x>
- Nong ATQ, Hauenberger CA, Gallhofer D, Skrzypek E, Dinh SQ (2022) Geochemical and zircon U-Pb geochronological constraints on late Mesozoic Paleo-Pacific subduction-related volcanism in southern Vietnam. *Mineral Petrol* 116:349–368. <https://doi.org/10.1007/s00710-022-00785-z>
- Neubauer F, Dallmeyer RD, Dunkl I, Schirnik D (1995) Late Cretaceous exhumation of the metamorphic Gleinalm dome, Eastern Alps: kinematics, cooling history and sedimentary response in a sinistral wrench corridor. *Tectonophysics* 242:79–98. [https://doi.org/10.1016/0040-1951\(94\)00154-2](https://doi.org/10.1016/0040-1951(94)00154-2)
- Parrish RR (1990) U-Pb dating of monazite and its application to geological problems. *Can J Earth Sci* 27:1431–1450. <https://doi.org/10.1139/e90-152>

- Parrish RR (2001) The response of mineral chronometers to metamorphism and deformation in orogenic belts. In: Miller JA, Holdsworth RE, Buick IS, Hand M (eds) Continental reactivation and reworking 184. Geol Soc Lond Spec Publ, London, pp 289–301
- Paton C, Hellstrom J, Paul B, Woodhead J, Hergt J (2011) Iolite: free-ware for the visualisation and processing of mass spectrometric data. *J Anal Spectrom* 26:2508–2518. <https://doi.org/10.1039/c1ja10172b>
- Pearce NJG, Perkins WT, Westgate JA, Gorton MP, Jackson SE, Neal CR, Chenery SP (1997) A compilation of new and published major and trace element data for NIST SRM 610 and NIST SRM 612 glass reference materials. *Geostand Geoanal Res* 21:115–144. <https://doi.org/10.1111/j.1751-908X.1997.tb00538.x>
- Petrík I, Broska I, Lipka J, Šiman P (1995) Granitoid allanite-(Ce): substitution relations, redox conditions and REE distributions (on an example of I-type granitoids, Western Carpathians, Slovakia). *Geol Carpathica* 46:79–94
- Puhr B (2013) Metamorphic evolution and geochemistry of metacarbonate rocks of the Austroalpine Basement (Eastern Alps). Dissertation, University of Graz
- Roberts MP, Finger F (1997) Do U-Pb zircon ages from granulites reflect peak metamorphic conditions? *Geology* 25:319–322. [https://doi.org/10.1130/0091-7613\(1997\)025<0319:DUPZAF>2.3.CO;2](https://doi.org/10.1130/0091-7613(1997)025<0319:DUPZAF>2.3.CO;2)
- Rubatto D (2017) Zircon: the metamorphic mineral. *Rev Mineral Geochem* 83:261–295. <https://doi.org/10.2138/rmg.2017.83.9>
- Ruiz Cruz MD, Sanz de Galdeano C, Alvarez-Valero A, Rodriguez Ruiz MD, Novák J (2010) Pumpellyite and coexisting minerals in metapelites and veins from the Federico units in the internal zone of the Rif, Spain. *Can Mineral* 48:183–203. <https://doi.org/10.3749/canmin.48.1.183>
- Schärer U (1984) The effect of initial ^{230}Th disequilibrium on young U-Pb ages: the Makalu case, Himalaya. *Earth Planet Sci Lett* 67:191–204. [https://doi.org/10.1016/0012-821X\(84\)90114-6](https://doi.org/10.1016/0012-821X(84)90114-6)
- Schaen AJ, Jicha BR, Hodges KV et al (2020) Interpreting and reporting $^{40}\text{Ar}/^{39}\text{Ar}$ geochronologic data. *Geol Soc Am Bull* 133:461–487. <https://doi.org/10.1130/B35560.1>
- Schlüter J, Tarkian M, Stumpf EF (1984) Die stratiforme Sulfdilagerstätte Walchen, Steiermark, Österreich: Geochemie und Genese. *Tschermaks Mineral Petrogr Mitt* 33:287–296
- Schmid SM, Fügenschuh B, Kissling E, Schuster R (2004) Tectonic map and overall architecture of the Alpine orogen. *Eclogae Geol Helvetica* 97:93–117. <https://doi.org/10.1007/s00015-004-1113-x>
- Schulz B (2017) Polymetamorphism in garnet micaschists of the Saualpe Eclogite Unit (Eastern Alps, Austria), resolved by automated SEM methods and EMP-Th-U-Pb monazite dating. *J Metamorph Geol* 35:141–163. <https://doi.org/10.1111/jmg.12224>
- Schuster R, Kurz W, Krenn K, Fritz H (2013) Introduction to the geology of the Eastern Alps. *Ber Geol Bundesanst Wien* 99:121–133
- Schuster R, Scharbert S, Abart R, Frank W (2001) Permo-Triassic extension and related HT/LP metamorphism in the Austroalpine—Southalpine realm. *Mitt Ges Geol Berbaustud Österr* 45:111–141
- Schuster R, Stüwe K (2008) Permian metamorphic event in the Alps. *Geol* 36:603. <https://doi.org/10.1130/G24703A.1>
- Seydoux-Guillaume AM, Goncalves P, Wirth R, Deutsch A (2003) Transmission electron microscope study of polyphase and discordant monazites: Site-specific specimen preparation using the focused ion beam technique. *Geology* 31:973–976. <https://doi.org/10.1130/G19582.1>
- Shaw DM (1956) Geochemistry of pelitic rocks. Part III: Major elements and general geochemistry. *Geol Soc Am Bull* 67:919–934. [https://doi.org/10.1130/0016-7606\(1956\)67\[919:GOPRPI\]2.0.CO;2](https://doi.org/10.1130/0016-7606(1956)67[919:GOPRPI]2.0.CO;2)
- Skrzypek E, Kato T, Kawakami T, Sakata S, Hattori K, Hirata T, Ikeda T (2018) Monazite behaviour and time-scale of metamorphic processes along a low-pressure/high-temperature field gradient (Ryoke Belt, SW Japan). *J Petrol* 59:1109–1144. <https://doi.org/10.1093/ptrology/egy056>
- Sláma J, Košler J, Condon DJ et al (2008) Plešovice zircon—a new natural reference material for U-Pb and Hf isotopic microanalysis. *Chem Geol* 249:1–35. <https://doi.org/10.1016/j.chemgeo.2007.11.005>
- Smith HA, Barreiro B (1990) Monazite U-Pb dating of staurolite grade metamorphism in pelitic schists. *Contrib Mineral Petrol* 105:602–615. <https://doi.org/10.1007/BF00302498>
- Smye AJ, Roberts NMW, Condon DJ, Horstwood MSA, Parrish RR (2014) Characterising the U-Th-Pb systematics of allanite by ID and LA-ICPMS: implications for geochronology. *Geochim Cosmochim Acta* 135:1–28. <https://doi.org/10.1016/j.gca.2014.03.021>
- Spear FS (2010) Monazite—allanite phase relations in metapelites. *Chem Geol* 279:55–62. <https://doi.org/10.1016/j.chemgeo.2010.10.004>
- Sterner SM, Pitzer KS (1994) An equation of state for carbon dioxide valid from zero to extreme pressures. *Contrib Mineral Petrol* 117:362–374. <https://doi.org/10.1007/BF00307271>
- Stumpf S (2023) From sedimentation to multiple tectono-thermal events: U/Pb detrital zircon and allanite age dating in the Eastern Alps. MSc thesis, Technical University of Graz
- Stüwe K (1998) Heat sources of cretaceous metamorphism in the Eastern Alps—a discussion. *Tectonophysics* 287:251–269. [https://doi.org/10.1016/S0040-1951\(98\)80072-3](https://doi.org/10.1016/S0040-1951(98)80072-3)
- Stüwe K, Schuster R (2010) Initiation of subduction in the Alps: continent or ocean? *Geol* 38:175–178. <https://doi.org/10.1130/G30528.1>
- Tenczer V, Stüwe K (2003) The metamorphic field gradient in the eclogite type locality, Koralpe region, Eastern Alps. *J Metamorph Geol* 21:377–393. <https://doi.org/10.1046/j.1525-1314.2003.00448.x>
- Tera F, Wasserburg GJ (1972) U-Th-Pb systematics in three Apollo 14 basalts and the problem of initial Pb in lunar rocks. *Earth Planet Sci Lett* 14:281–304. [https://doi.org/10.1016/0012-821X\(72\)90128-8](https://doi.org/10.1016/0012-821X(72)90128-8)
- Thöni M, Miller C, Blichert-Toft J, Whitehouse MJ, Konzett J, Zanetti A (2008) Timing of high-pressure metamorphism and exhumation of the eclogite type-locality (Kupplerbrunn–Prickler Halt, Saualpe, south-eastern Austria): constraints from correlations of the Sm-Nd, Lu-Hf, U-Pb and Rb-Sr isotopic systems. *J Metamorph Geol* 26:561–581. <https://doi.org/10.1111/j.1525-1314.2008.00778.x>
- Vermeesch P (2018) IsoplotR: a free and open toolbox for geochronology. *Geosci Front* 9:1479–1493. <https://doi.org/10.1016/j.gsf.2018.04.001>
- Villa IM, Glodny J, Peillod A, Skelton A, Ring U (2022) Petrochronology of polygenetic white micas (Naxos, Greece). *J Metamorph Geol* 41:401–423. <https://doi.org/10.1111/jmg.12700>
- Wendt I, Carl C (1991) The statistical distribution of the mean squared weighted deviation. *Chem Geol* 86:275–285. [https://doi.org/10.1016/0168-9622\(91\)90010-T](https://doi.org/10.1016/0168-9622(91)90010-T)
- White RW, Powell R, Holland TJB (2007) Progress relating to calculation of partial melting equilibria for metapelites. *J Metamorph Geol* 25:511–527. <https://doi.org/10.1111/j.1525-1314.2007.00711.x>
- White RW, Powell R, Holland TJB, Johnson TE, Green ECR (2014) New mineral activity-composition relations for thermodynamic calculations in metapelitic systems. *J Metamorph Geol* 32:261–286. <https://doi.org/10.1111/jmg.12071>
- Whitney DL, Evans BW (2010) Abbreviations for names of rock-forming minerals. *Am Mineral* 95:185–187. <https://doi.org/10.2138/am.2010.3371>

- Wiedenbeck M, Allé P, Corfu F, Griffin WL, Meier M, Oberli F, Von Quadt A, Roddick JC, Spiegel W (1995) Three natural zircon standards for U-Th-Pb, Lu-Hf, trace element and REE analyses. *Geostand Geoanal Res* 19:1–23. <https://doi.org/10.1111/j.1751-908X.1995.tb00147.x>
- Wiesinger M, Neubauer F, Handler R (2006) Exhumation of the Saualpe eclogite unit, Eastern Alps: constraints from $^{40}\text{Ar}/^{39}\text{Ar}$ ages and structural investigations. *Mineral Petrol* 88:149–180. <https://doi.org/10.1007/s00710-006-0154-4>
- Wing BA, Ferry JM, Harrison TM (2003) Prograde destruction and formation of monazite and allanite during contact and regional metamorphism of pelites: petrology and geochronology. *Contrib Miner Petrol* 145:228–250. <https://doi.org/10.1007/s00410-003-0446-1>
- Yakymchuk C (2023) Prograde zircon growth in migmatites. *J Metamorph Geol* 41:719–743. <https://doi.org/10.1111/jmg.12715>

Publisher's Note Springer Nature remains neutral with regard to jurisdictional claims in published maps and institutional affiliations.